Probing *ultra-slow* magnetisation relaxation in transition metal fluorides through DC and AC magnetometry

A Thesis

submitted to

Indian Institute of Science Education and Research Pune
in partial fulfillment of the requirements for the
BS-MS Dual Degree Programme

by

Shashwat Singh Tomar

Indian Institute of Science Education and Research Pune
Dr. Homi Bhabha Road,
Pashan, Pune 411008, INDIA.

April, 2023

Supervisor: Dr. Ashna Bajpai
© Shashwat Singh Tomar   2023

Certificate

This is to certify that this dissertation entitled Probing *ultra-slow* magnetisation relaxation in transition metal fluorides through DC and AC magnetometry towards the partial fulfilment of the BS-MS dual degree programme at the Indian Institute of Science Education and Research, Pune represents study/work carried out by Shashwat Singh Tomar at Indian Institute of Science Education and Research under the supervision of Dr. Ashna Bajpai, Associate Professor, Department of Physics, during the academic year 2022-2023.
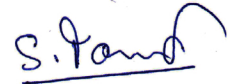
Dr. Ashna Bajpai

Committee:

Dr. Ashna Bajpai

Dr. Sunil Nair

This thesis is dedicated to my parents and my sister

Declaration

I hereby declare that the matter embodied in the report entitled Probing *ultra-slow* magnetisation relaxation in transition metal fluorides through DC and AC magnetometry are the results of the work carried out by me at the Department of Physics, Indian Institute of Science Education and Research, Pune, under the supervision of Dr. Ashna Bajpai and the same has not been submitted elsewhere for any other degree.

Shashwat Singh Tomar

Acknowledgments

Lastly I would like to thank my family for all the love they have given me. My dad for his unwavering support and affection, my mom for providing encouragement and comfort, and my sister for her resolute guidance.

Abstract

Certain antiferromagnets (AFMs) show the phenomenon of spin canting when it is symmetry allowed. Aside from being responsible for exotic spin structures like skyrmions, the phenomenon of weak ferromagnetism also shows a potential for technological applications in next generation devices. This project aims to investigate a very specific trait that pertains to an ultra-slow magnetization relaxation phenomenon observed in a number of Dzyaloshinskii-Moriya Interaction (DMI) driven AFMs through Superconducting Quantum Interference Device (SQUID) magnetometry. In this project, our aim is to investigate whether such unique magnetization dynamics is also shown by Single Ion Anisotropy (SIA) driven spin canted systems which are also symmetry allowed piezomagnets. For this purpose we have explored two of these SIA driven Weak Ferromagnets (WFMs), NiF_2 and CoF_2, in powders consisting of regular shaped micro-crystallites & in Single Crystal (SC) form. The microcrystals are prepared using solvothermal route by Sri Pragna in our lab. The single crystals of CoF_2 and NiF_2 have been provided by Dr. D. Prabhakaran, Oxford Physics.

The Thermo-remanent Magnetization (TRM) in NiF_2 and CoF_2 microcrystallites, obtained through SQUID magnetometry, is presented in this thesis. These data show ultra-slow magnetization relaxation dynamics which is intimately connected to the spin canted phase. This enigmatic result is strikingly similar to previous results on DMI driven WFMs, however, unlike the DMI driven WFMs, the TRM does not show a peak when its magnetic field variation is investigated, at least for field till 10 kOe. Analysis of the DC magnetometry data reveals that spin canting appears to play an important role in the magnetization dynamics of not only NiF_2, but also CoF_2. The inverse susceptibilities for both the samples show huge deviations from linearity in the paramagnetic region. This deviation exists much away from the magnetic transition region, wherein deviations from linearity due to correlations are typically not observed.

To further investigate the magnetization relaxation, AC-Susceptibility data on CoF_2 SC is taken. AC-Susceptibility is one of the best-known techniques for probing relaxation phenomenon. Towards this, a fully functional Liquid Helium (LHe) compatible AC-Susceptometer was constructed, and AC-Susceptibilty data on these SCs above 77 K (Liquid Nitrogen (LN_2) temperature) was obtained. The construction of the AC-Susceptometer involved designing a LHe compatible insert with coils wound on the Quartz tubes themselves for improved sensitivity (by about 1.6 times). This is noteworthy, as winding of secondary

in the double walled glass-insert itself – which makes sample closer to the secondary coil – is not reported before to the best of our knowledge. This is extremely significant, especially if AFMs are to be probed. This work endeavors to summarize this, and other peculiar results.

Contents

List of Figures

List of Tables

Chapter 1

Introduction

Spin canting in certain Antiferromagnets (AFMs) is an interesting phenomenon that has amassed popularity in recent years. These spin canted AFMs are also known as Weak Ferromagnets (WFMs). Spin canting is found in various magnetic materials such as multiferroics, topological insulators etc. [1], [2], and is widely used to explain the properties of spin textures like skyrmions [3] and spin spirals [4]. A well-known mechanism for spin canting is that of Dzyaloshinskii Moriya Interaction (DMI). DMI has gained significance from both fundamental and application point of view. We have a observed a peculiar trait in remanence in these DMI driven WFMs which appears to be fundamentally different from the remanence observed in routine Ferromagnets (FMs), AFMs or even spin glasses. [5]–[8]

Spin canting in AFMs is also known to occur through another mechanism know as Single Ion Anisotropy (SIA). This project aims to investigate two of these spin canted systems, namely NiF_2 and CoF_2 which are driven by SIA. Both these systems are also symmetry allowed piezomagnets (PzMs) [9], [10], though piezomagnetism has been a much less explored phenomenon. We have investigated both these systems using remanence (through SQUID magnetometry) as well as AC magnetometry.

The AFM vector of NiF_2 is in the basal plane [11]. Spin canting is seen to occur without any external pressure. On the contrary, CoF_2 is primarily a PzM which shows weak ferromagnetism under external stress [10]. The origin of spin canting in this compound is not clear, especially whether it is due to the inequivalence of sub-lattice magnetization [10], [12], [13], or due to any other mechanism. It is interesting to note that the remanence data ob-

tained on powder samples discussed in chapter 2 appears to show signatures of spin canting without any external stress.

In this work we have analyzed SQUID magnetization data on the micro-crystalline NiF_2 and CoF_2 samples. These samples were synthesized in the lab by Sri Pragna Dubbaku. Both of these show opening of the loop in M-H isotherm similar to WFM. Besides the regular magnetization data, the TRM data on both these compounds is also looked at. TRM helps discern properties of WFMs which are not immediately evident from regular M-H isotherms and Magnetization as a function of Temperature (M vs T) measurements. The results obtained on the TRM data of these SIA driven WFMs are strikingly similar to that obtained in other DMI driven WFMs such as α-Fe_2O_3, $MnCO_3$ and $FeCO_3$ [8]. Similar to earlier observations, both samples exhibit two different time scales in TRM relaxation measurement, the first is an instantaneous decay and the second is a quasi-static part resulting in *time-stable remanence* [7], [8]. The susceptibilities of these samples are FM like, and a huge non-linearity in the paramagnetic region is noteworthy.

Previous works on DMI-driven WFMs [5]–[8] suggest that this slow relaxation phenomenon is fundamentally different from relaxation in routine FMs & AFMs. Therefore, to probe these systems further, AC susceptibility appears to be the most suitable technique. Non-linear susceptibility is an excellent tool to differentiate between different magnetic orders, and characterize magnetic the system. This has already been used to probe superconductors, spin glasses, single molecular magnets, superparamagnets etc. [14], [15] To learn more about AC susceptibility, extensive time was spent learning about the setup both theoretically and experimentally. A Liquid Helium (LHe) compatible AC-Susceptometer setup was then constructed, characterised, and calibrated by using two paramagnetic salts, Gd_2O_3 and Er_2O_3. The field profile as a function of the current passed through it is also looked at for the primary coil constructed. Finally, AC susceptibility data on CoF_2 SC above 77 K was also collected. While the insert of LHe is designed and fabricated, the actual LHe run could not be performed due to lack of time.

Below are discussed some fundamentals of magnetization and magnetic materials which are important for understanding the results discussed in this thesis.

1.1 Magnetism in Materials

Magnetism in materials comes from a fundamental entity called the magnetic moment, μ. The energy, E, associated with it when it is placed in a magnetic field, $\mathbf{B}$, is given by –

$$E = -\mu \cdot \mathbf{B} \tag{1.1}$$

Electrons in materials contain an intrinsic spin magnetic moment and also an orbital magnetic moment which depends on the electronic configuration of a material. Although there is no classical counterpart to the spin part, this can be thought of as akin to the moment produced due to a charged body spinning about its own axis and rotating about another. Due to the combined effect of spin and orbital moment, atoms in a material possess magnetic moments, and this gives rise to a magnetization, $\mathbf{M}$. Here, $\mathbf{M}$ is the magnetic moment per unit volume [16].

In a magnetic material, the magnetic field can be described by $\mathbf{B}$ and $\mathbf{H}$. These vector fields are linearly related as –

$$\mathbf{B} = \mu_0(\mathbf{H} + \mathbf{M})$$

Here, μ_0 is called the permeability of free space. It has a value $4\pi \times 10^{-7}$ Hm^{-1}. But, in linear materials, $\mathbf{M} = \chi\mathbf{H}$, where χ is the linear magnetic susceptibility of the material. As we will see later, when an AC field is applied, this can be either real or imaginary depending on whether it is in phase or out of phase with the applied field. This gives us the relation –

$$\mathbf{B} = \mu_0(\chi + 1)\mathbf{H}$$

This is only strictly valid when $\chi << 1$. Hence, $|\mathbf{M}| << |\mathbf{H}|$, and the internal fields inside the solid are nearly equal to the external fields [16].

The orbital angular momentum of electrons is characterised by the quantum numbers l and $m_l = l\hbar, (l-1)\hbar, ..., -l\hbar$, which for an electron, depend on the electronic configuration of the atom. Its magnitude is given by $\sqrt{l(l+1)}\hbar$, and its component along a particular axis (say z-axis) is given by $m_l\hbar$. The magnitude of the orbital magnetic moment is $\sqrt{l(l+1)}\mu_B$ and its component along z-axis is $-m_l\mu_B$. Similarly, the spin angular momentum is characterised by the quantum numbers s and $m_s = s\hbar, (s-1)\hbar, ..., -s\hbar$. Its magnitude is $\sqrt{s(s+1)}\hbar$ and the component along z-axis is $m_s\hbar$. The value of s for an

electron is 1/2, therefore, $m_s = \pm 1/2$. The magnitude of spin magnetic moment is therefore $\sqrt{s(s+1)}g\mu_B = \sqrt{3}g\mu_B/2$ and its component along z-axis is $-g\mu_B m_s = \mp g\mu_B/2$. Here, g is the spin g-factor, which has a value nearly equal to 2, and $\mu_B = 9.27 \times 10^{-24}$ JT^{-1} is the Bohr magneton [16].

1.2   Crystal Field and Orbital Quenching

The arrangement of anions (ligands) around a magnetic ion produces a particular electric field which is called the crystal field. In crystal field theory, the crystal field effects depend on the symmetry of the local environment around the magnetic ion. Two common cases are those of tetrahedral and octahedral environments, the latter being present in both NiF_2 and CoF_2. Fig(1.1a) denotes the octahedral environment and the energy level splitting of the d-orbitals of the magnetic ion due to the electrostatic interactions with the ligands [16].

In 3d orbital ions, the spin-orbit coupling is much weaker than the crystal field interactions. It has been observed that the system hence chooses a ground state such that the orbital angular momentum, $L = 0$, and the total angular momentum is just the spin angular momentum, S. Therefore, the orbital angular momentum is quenched and this is called orbital quenching (many materials show partial quenching which then is accounted for by taking a g-value greater than 2). This is not valid for 4f ions since these orbitals are buried deep inside the atoms and the crystal field interaction is much less [16].

1.3   Exchange Interactions

1.3.1   Direct Exchange

In direct exchange, the electrons on two neighbouring magnetic atoms interact through exchange interaction without the need for an intermediary atom. Even for d-orbital electrons, let alone the f-orbital ones (which are buried deeper in the atom), the overlap of orbitals is not enough to justify a long-range order based on just direct exchange interaction [16].

8
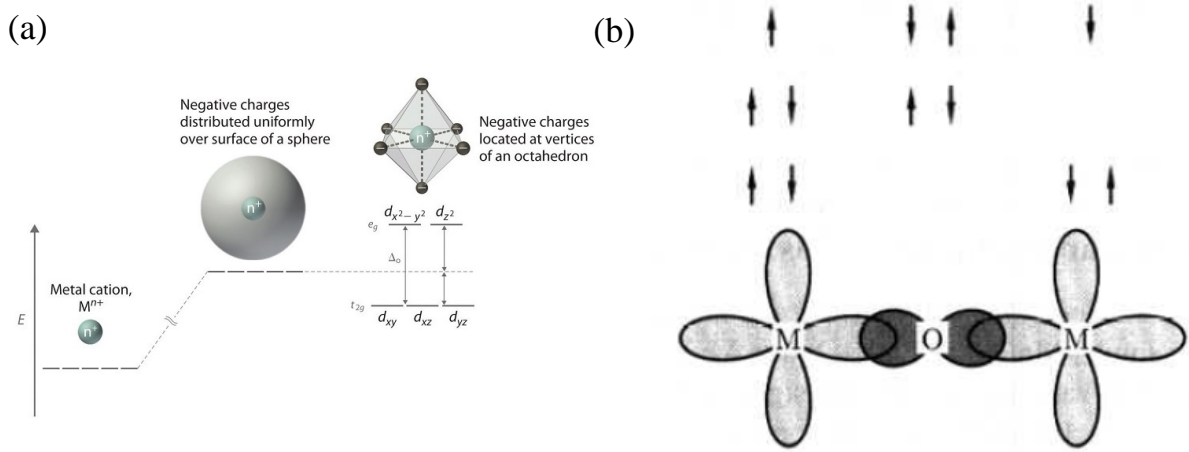
Figure 1.1: (a) Octahedral crystal field and the associated energy level splitting of the orbitals [17]. (b) Superexchange interaction [16].

1.3.2 Long-range Magnetic Ordering

The magnetic moments associated with each ion in a material interact with each other not just by dipole-dipole interactions, but quantum mechanically. These are called exchange interactions and are the essence behind long-range magnetic ordering in materials. They are of various types and typically depend on the separation between magnetic ions and their geometrical arrangement. Since the energy would depend on the interaction of spins, and it goes as dot product between the moment and the field (Eq(1.1)), a Hamiltonian can be defined to model the exchange interactions –

$$\hat{\mathcal{H}} = -\sum_{j,k} J_{j,k} \mathbf{S_j} \cdot \mathbf{S_k}$$

Here, $J_{j,k}$ is the exchange constant between the jth and the kth spin, $\mathbf{S}$. For two electrons on the same atom, the coulomb repulsion is minimised by keeping 'J' positive. This favours a triplet state (both spins in the same direction), and hence an anti-symmetric spatial state which keeps the electrons farther apart [16], [18].

Superexchange in Ions

This type of interaction acts between two non-neighbouring magnetic ions, through a non-magnetic intermediary ion. In Fig(1.1b), the magnetic ions have one unpaired electron, while the non-magnetic middle ion has fully occupied orbitals. Here, because of Pauli exclusion principle, an anti-ferromagnetic coupling is favoured and the electrons are delocalized over the entire structure. This can be thought of a particle in a box problem, hence their kinetic energy is reduced due to bigger spatial occupancy. This interaction is strongly dependent on the degree of orbitals overlap and the bond angles. It occurs in MnF_2, MnO, and also in both NiF_2 and CoF_2.

Superexchange can sometimes also be ferromagnetic. If an electron hops from one orbital to an unoccupied orbital, it is favourable for its spin to be aligned with that of other electrons in the atom to reduce Coulomb repulsion. Hence, the ions will show ferromagnetic coupling [16], [18].

Double Exchange

This kind of interaction can occur in oxides where the magnetic ions at two or more different lattice sites show different valencies. It results in a ferromagnetic coupling between the ions. As an example, in $La_{1-x}Sr_xMnO3$, the e_g electron of the Mn^{3+} ion hops to the empty e_g orbital of Mn^{4+} ion. Then according to the Hund's rule it should have its spins aligned to those in the Mn^{4+} ion to reduce Coulomb repulsion. Thus, a ferromagnetic alignment takes place. This hopping then also causes the material to become metallic. This corresponds to superexchange interaction in an extended system instead of just two isolated ions. This is found in a variety of materials like magnetite (Fe_3O_4), $La_{1-x}Sr_xMnO3$, etc [16], [18].

1.4 Basic Types of Magnetic Ordering

1.4.1 Diamagnetism

Diamagnetism is the property of showing a weak negative susceptibility. This is present in all materials but is significantly overshadowed, as far as magnitude of this effect is concerned, when some unpaired electrons are present. In these materials, a magnetic moment which opposes the applied magnetic field, **B**, is induced (Fig(1.2(a))). Some examples of diamagnetic solids are NaF, NaCl, KBr, etc [16], [18].

1.4.2 Paramagnetism

Paramagnetism refers to the property of magnetic moments to line up along the applied magnetic field's direction. These materials have a positive susceptibility and a magnetization in the field's direction is obtained. The atoms/ions here have unpaired electron(s) present which give each ion a magnetic moment. These moments point in random directions in the absence of an external field and don't interact with each other sufficiently, hence, exchange interactions can be ignored here.

Consider a magnetic field, **B**, in the z-direction and a moment, μ, associated with each atom. This would produce a magnetization in the z-direction. Then –

$$\frac{\langle \mu_z \rangle}{\mu} = \coth y - \frac{1}{y}$$

Where, $y = \mu B / k_B T$. But –

$$\coth y = \frac{1}{y} + \frac{y}{3} + O(y^3)$$

This gives –

$$\chi \approx \frac{\mu_0 M}{B} = \frac{\mu_0}{B} \frac{M_s \langle \mu_z \rangle}{\mu} \approx \frac{N \mu_0 \mu^2}{3 k_B T}$$

Where, the material contains total N atoms, and, $M_s = N\mu$ is the saturation magnetization of the material. This tells us that the susceptibility, χ, is positive and inversely proportional to the temperature, T. This is known as the Curie's law. This is valid when B, and hence M, is small enough so that $O(y^3)$ terms can be ignored [16].
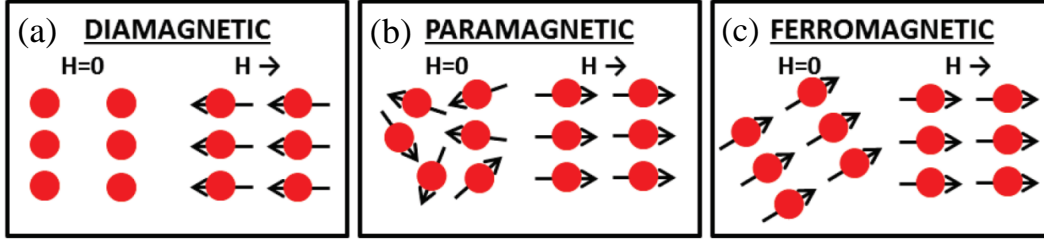
Figure 1.2: Schematic representation of (a) Diamagnetism, (b) Paramagnetism and (c) Ferromagnetism [19].

1.4.3 Ferromagnetism

In a ferromagnet, below a certain temperature, the neighbouring atoms all align in the same direction spontaneously without the application of an external magnetic field. This temperature, T_C, is known as the Curie Temperature, and demarcates the phase transition between the ferromagnetic and the paramagnetic phases. Even below T_C, due to the presence of domains (regions in which all the moments are aligned parallel in the same direction) in the material, the magnetization is usually not visible on the macroscopic level. When an external field, **B**, is applied, the Hamiltonian is –

$$\hat{\mathcal{H}} = -\sum_{j,k} J_{j,k}\mathbf{S_j} \cdot \mathbf{S_k} + g\mu_B \sum_j \mathbf{S_j} \cdot \mathbf{B} \tag{1.2}$$

Here, the exchange constant $J_{j,k}$ is positive. The second term is the Zeeman energy. At T>T_C, the susceptibility –

$$\chi \propto \frac{1}{T - T_C}$$

This is known as the Curie Weiss law and is valid when B, and hence magnetization, M, is small enough [16].
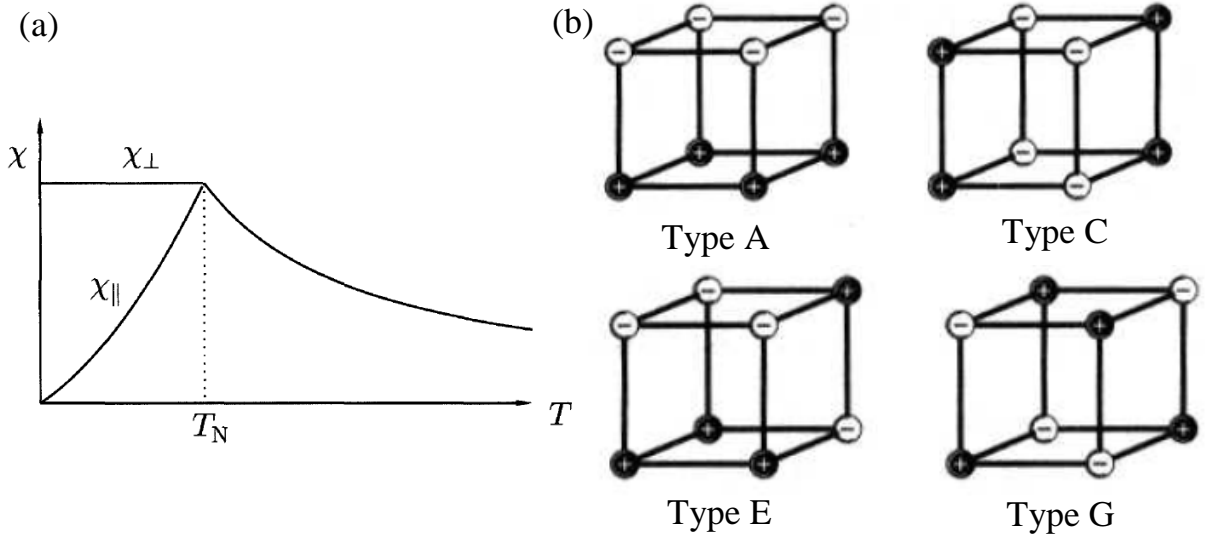
Figure 1.3: (a) Typical DC susceptibility of an AFM in low field. (b) Types of AFMs [16].

1.4.4 Antiferromagnetism

In antiferromagnetic materials, the exchange constant, $J_{j,k}$, is negative. Below a certain temperature, T_N, this therefore favours the nearest neighbour moments to lie opposite to each other. Here T_N, the Néel Temperature, demarcates the phase transition between the AFM and the paramagnetic phases. These can often be considered as consisting to two interpenetrating sub-lattices having opposite magnetization. Similar to the FM susceptibility, for $T > T_N$, the susceptibility –

$$\chi \propto \frac{1}{T + T_N}$$

But for AFMs the predicted T_N from paramagnetic susceptibility is often very different from the actual T_N. Fig(1.3a) shows the susceptibility, χ, as a function of temperature in the presence of a weak field. The antiferromagnetic order can also be of various types, since opposite spins can be arranged in a lattice in many different ways. This is shown in Fig(1.3b). Some common AFMs are NiF_2, MnO, α-Fe_2O_3, CoF_2, etc [16].

1.4.5 Weak Ferromagnetism

Weak ferromagnetism is the spontaneous magnetization in certain AFMs due to spin canting. The magnetization in these crystals is nearly $10^{-2} \sim 10^{-3}$ times the nominal value [12]. Dzyaloshinskii first came up with a phenomenological theory of spin canting based on thermodynamic theory of transitions and from crystal symmetry considerations [20]. Building on this, Moriya developed the theory of anisotropic superexchange interaction by taking spin-orbit coupling into account [21]. Two kinds of phenomena are responsible for weak ferromagnetism – anisotropic spin-spin coupling, which is DMI, and SIA [12].

Symmetry Considerations

In 1957, Dzyaloshinskii gave a phenomenological argument, 'for a spontaneous magnetic moment m to exist, it must be invariant under the action of all transformations of the symmetry of the crystal class'. When considering ionic spins, there exists an additional symmetry element R, which changes the sign of the spins from s(x, y, z) → –s(x, y, z). Thus, while discussing the symmetries of spin distributions, 'magnetic space groups' and 'magnetic point groups' are used [20].

Consider the case of NiF_2. From Fig(1.4a) it can be seen that the spins point along the a or the b-axis. Here, for spin canting in the ab-plane (001), the canted spin arrangement has the same symmetry as AFM spin arrangement. This also means that there is a magnetic moment vector **m** which is invariant under all the symmetry transformations of the magnetic space group [12]. Therefore, NiF_2 shows weak ferromagnetism, with m perpendicular to the c-axis.

Dzyaloshinskii-Moriya Interaction (DMI)

In its most extensive form, the bilinear spin-spin coupling between two spins S_1 and S_2 may be formulated as [12]—

$$V_{12} = \mathbf{S_1} \cdot K_S \cdot \mathbf{S_2} + \mathbf{S_1} \cdot K_A \cdot \mathbf{S_2}$$
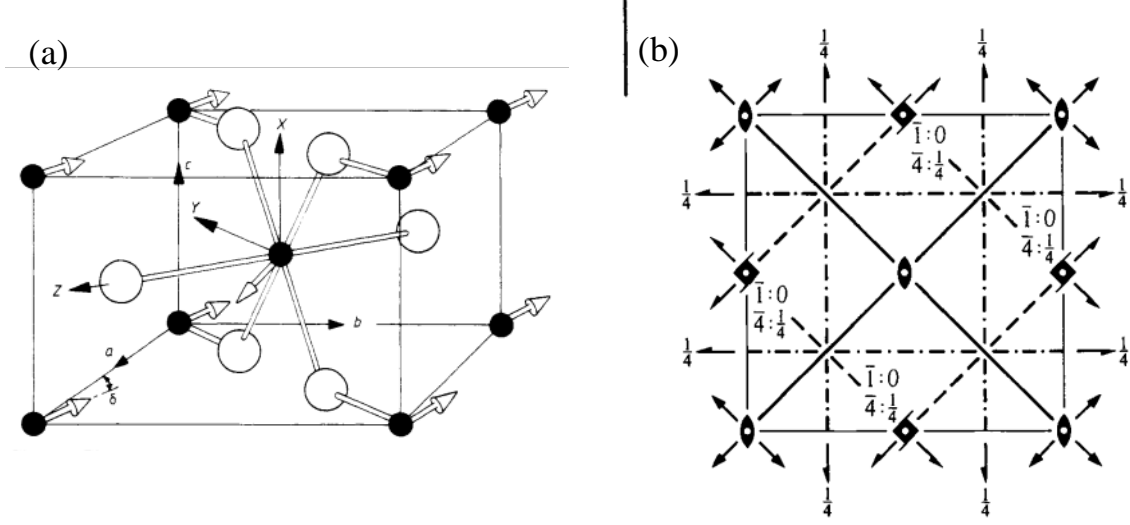
Figure 1.4: (a) Tetragonal unit cell of NiF_2 (rutile structure). Arrows indicate the direction of magnetic moment on Ni^{2+} [22] (b) The P42/mnm space group [23].

Here K_S and K_A represent the symmetrical and anti-symmetrical tensors respectively. The symmetrical part in the above coupling can always be written as [12]—-

$$K_\alpha S_{1\alpha} S_{2\alpha} + K_\beta S_{1\beta} S_{1\beta} + K_\gamma S_{1\gamma} S_{1\gamma}$$

by properly choosing a set of coordinate axes α, β, and γ. Here k_α can be chosen as the largest amongst all three coefficients without loss of generality. Then, in its most conducive orientation, the AFM spins would be directed along the α-direction. Hence, spin canting is not possible from the symmetrical part of the spin coupling in two sublattice AFMs. The anti-symmetric part can be expressed as [12]—

$$\mathbf{D} \cdot [\mathbf{S_1} \times \mathbf{S_2}] \qquad (1.3)$$

Where $\mathbf{D}$ is the constant DMI vector, and $\mathbf{S_1}$, $\mathbf{S_2}$ are the magnetic moments of the two magnetic sublattices under consideration. It can be easily seen that the minimum occurs when the two spins are perpendicular to one another. Hence it is this anti-symmetric term which acts to cant the spins [12].

Single Ion Anisotropy

SIA is an energy term in the Hamiltonian due to the crystalline electric field. It is one of the fine structure energies and the lowest order terms are quadratic in spin operators —

$$\lambda^2(\alpha S_x^2 + \beta S_y^2 + \gamma S_z^2)$$

Where λ denotes the strength of the interaction and α, β, and γ are given by second order perturbative approximation. These again are usually determined by experimental methods. Since SIA is independent of the exchange energy, its manifestations can be seen above the magnetic transition temperature. It is also expected to play an important role in certain WFMs with low T_N [12].

Spin Hamiltonian for NiF_2 —

The orthorhombic environment of the corner (1) and the center (2) Ni^{2+} ions is at an angle of 90 degrees with each other about the c-axis. Hence, their easy axes are also perpendicular. Taking [110], [1$\bar{1}$0], and [001] directions as the x, y and z-axes, respectively —

$$\hat{\mathcal{H}} = -\sum_{j,k} J_{j,k} \mathbf{S_j} \cdot \mathbf{S_k} + \sum_{j}^{(1)} \{GS_{jz}^2 - E(S_{jx}^2 - S_{jy}^2) + \mu_B \mathbf{S_j} \cdot g_j \cdot \mathbf{H}\}$$

$$+ \sum_{k}^{(2)} \{GS_{kz}^2 + E(S_{kx}^2 - S_{ky}^2) + \mu_B \mathbf{S_k} \cdot g_k \cdot \mathbf{H}\}$$

Where again, the first term is the isotropic superexchange interaction, while the second and third terms are the SIA and the Zeeman energy respectively. The anisotropic spin-spin couplings were ignored as they have small magnitude (order $\sim 10^{-4} \cdot J$). It can be seen from above that SIA is negative when spin of ion (1) is canted towards x-axis and that of ion (2) towards y-axis. Hence, the energy is reduced in this configuration than when they are anti-parallel. Also, since the spins are perpendicular to the c-axis, the sign of G is expected to be positive, or E is expected to be sufficiently greater than $|G|$ [12], [24].

1.5 Piezomagnetism

In Piezomangnets (PzMs) an external force applied on the crystal can lead to the creation of a net magnetic moment. For a PzM, the magnetization in the i direction, M_i, in the absence of a magnetic field is –

$$M_i = \Lambda_{ijk}\sigma_{jk}$$

Here, Λ_{ijk} is the piezomagnetic tensor of order 3, and σ_{jk} is the usual stress tensor. Hence, when a stress σ_{jk} is applied, a magnetic moment linear to it is produced. The prototypical examples of PzM are α-Fe_2O_3 and CoF_2 [25].

1.5.1 Weak Ferromagnetism in CoF_2

The spins in CoF_2 are known to point along the c-axis [26]. Under stress, piezomagnetic moments (both parallel to [001] and perpendicular to it) are observed. The origin appears to be related to the imbalance of magnetizations of the center and corner Co^{2+} ions. When $\sigma_{xy} = \sigma_{yz} = 0$ and $\sigma_{xz} \neq 0$, the AFM vector turns in the shear plane and a magnetic moment perpendicular to it is produced (i.e. along the y-axis). In contrast, when $\sigma_{xy} \neq 0$, then the AFM vector remains along c-axis, but a magnetic moment along c-axis owing to the imbalance of magnetization of two sub-latiices is produced [10].

Interestingly, in CoF_2 linear magnetostriction has been observed. In this case, when H is greater than 20 kOe, there is a jump in the linear magnetostriction and it changes its sign. This is the result of transition from one domain state to another in which the antiferromagnetic vector also changes its sign (but has same direction). The magnetization produced is found to be linearly proportional to H, at least for fields till 40 kOe, both parallel and perpendicular to [001]. For H > 40 kOe, when applied parallel to [001], the antiferromagnetic vector (L) rotates from a state parallel to [001] to a state perpendicular to it. When H is parallel to [110] and < 40 kOe, L is observed to rotate in the $(1\bar{1}0)$ plane, and there is magnetization parallel to both [110] and [001]. In short, the magnetization in CoF_2 is quite complicated, but is mostly linear in all directions for H < 40 kOe [13], [27].

1.6　Measurement Techniques

There are a variety of magnetization measurement techniques which can be used to probe different magnetic phases, associated time scales, microscopic or macroscopic properties, etc. of a system. Discussed below are two different experimental techniques to probe magnetic systems on macroscopic scale, but at different time scales. Both of these are used to probe the NiF_2 and CoF_2 samples and to find some peculiar features related to these WFM in these systems.

1.6.1　Superconducting Quantum Interference Device (SQUID) Magnetometer

SQUID is a widespread experimental technique that is used very frequently in almost all fields. It is a construct based on superconducting loop and Josephson junctions, and has been a key instrument in developing ultra-sensitive electric and magnetic measurement systems. It has demonstrated field resolutions of up to 10^{-17} T (quantum limited sensitivity) when operating at cryogenic temperatures [28]. SQUIDs find use in a variety of places, from detection of gravitational waves to measurement of magnetic fields in brain. SQUIDs function on three fundamental principles – superconductivity, Josephson effect and phase/flux quantization around a superconducting loop [29].

Superconductivity

Below a particular transition temperatures (T_C), certain materials undergo a transition to a superconducting state, which is marked by a complete lack of electrical resistance and perfect diamagnetism. The BCS theory tells that this absence of resistance is due to the formation of cooper pairs (bound state of two electrons) which can travel inside the material without scattering. These electrons can be de-paired by thermal, kinetic or magnetic interactions. Hence the superconductor has a critical temperature (T_C), a critical current density (J_C) and a critical field (H_C) above which it loses superconductivity. A full superconducting material can be described just by a single wavefunction [30], $\Psi = n_S e^{i\phi}$, where n_S is some pre-factor and ϕ is the phase [28], [29].
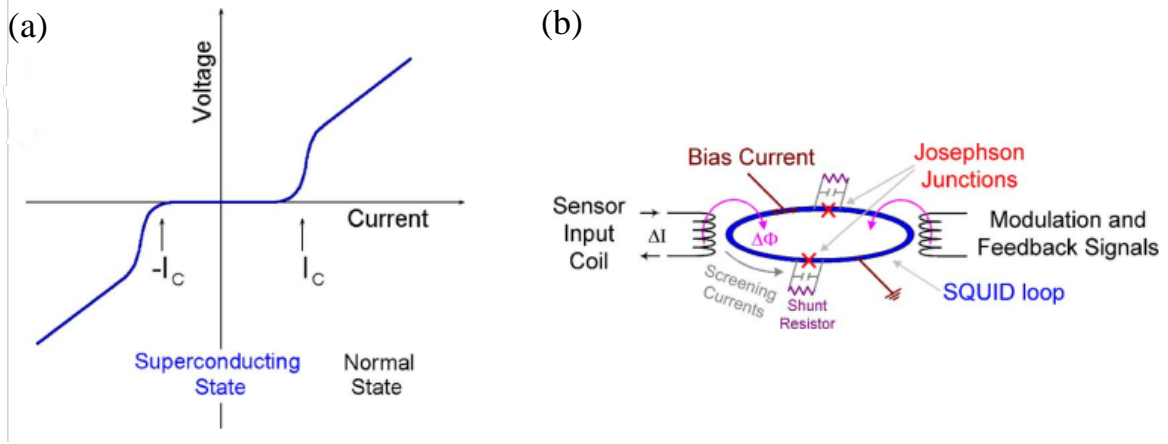
Figure 1.5: (a) I-V characteristic of a shunted Josephson junction [28]. (b) A DC SQUID loop. The capacitors represent internal capacitance of the SQUID [28].

Josephson Effect

If a resistive material is put in between two superconducting materials, and it is less than a characteristic coherent length (ξ) in width, the cooper pairs can 'tunnel' through it without any resistance. However, it is valid only for currents less than I_C, which is a characteristic of the resistive material. This combination of a resistive material between two superconductors forms a Josephson junction. A schematic I-V characteristic of a Josephson junction is shown in Fig(1.5a). The current across the junction can be written as [30] $I_S = I_C \sin(\Delta\phi)$, where $\Delta\phi$ is the phase difference between the two superconducting materials [28], [29].

Phase/ Flux quantization

If a ring is formed out of a superconducting material, the wavefunction at any point after a full loop must have phase difference of $2n\pi$, where n is any integer. This is known as phase quantization. Changing the flux inside a superconducting ring changes the phase of the wavefunction in a continuous manner. However, since the phase can only change in integer multiples of 2π, it leads to the quantization of flux inside a superconducting ring. Flux inside a superconducting ring is said to be trapped in discrete levels, integer multiple of the flux quantum, $\Phi_0 = 2.068 \times 10^{-15} W$ [28], [29].
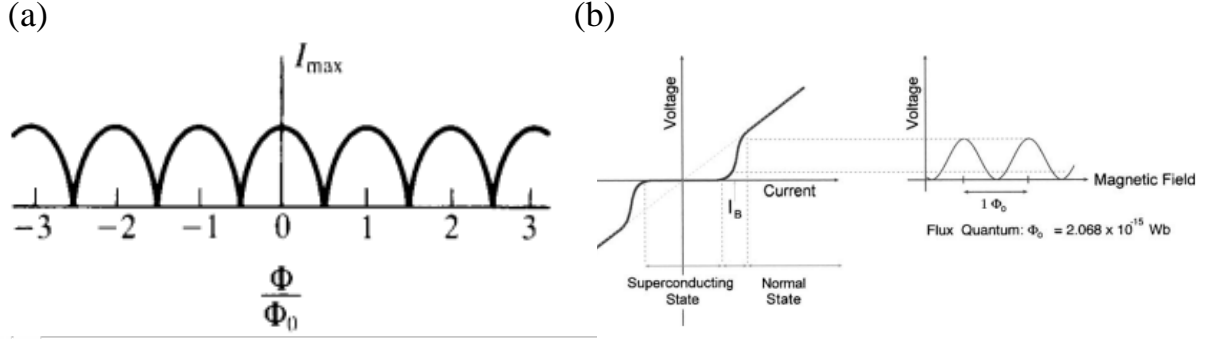
Figure 1.6: (a) Change in I_m as the flux Φ changes [30]. (b) Change in voltage (as I_S/I_B changes) with applied flux [28].

DC SQUID

SQUIDs use the above three fundamental principles to measure minute variations in magnetic field. The DC SQUID consists of two Josephson junctions in a superconducting ring which are shunted with a resistor to avoid hysteresis (Fig(1.5b)). When a magnetic field is applied through this ring, it evolves the phase differences between the two Josephson junctions such that the total phase around the ring is quantized. This leads to the equation [30] –

$$\phi_1 - \phi_2 = 2\pi\Phi/\Phi_0 (mod 2\pi)$$

Where ϕ_1 and ϕ_2 are the phase differences across the 1st and the 2nd Josephson junctions respectively, and Φ is the total flux contained in the ring $= \Phi_{screening} + \Phi_{external}$. As $\Phi_{external}$ changes, so does Φ, and this causes ϕ_1 and ϕ_2 to evolve with respect to one another such that the maximum supercurrent (I_m) has a simple trigonometric relation [30] –

$$I_m = 2I_C|\cos(\pi\Phi/\Phi_0)|$$

Here I_m can actually be thought of as the critical current I'$_C$ of the SQUID. This setup is now biased with a current little greater than $2I_C$ (where I_C is the critical current of one Josephson junction), putting it somewhere between superconducting and resistive behavior. This produces a voltage across the SQUID. When Φ changes, I'$_C$ evolves periodically with time, and this causes the associated voltage to also change periodically (with a period of the flux quantum Φ_0) (see Fig(1.6)). By measuring this change in voltage, one can measure the associated change in the flux coupled into the SQUID, and hence the magnetization of any

20

material [28], [29].

1.6.2   AC Susceptibility

AC susceptibility measurement is an important experimental technique typically used to study superconductivity, spin glasses, etc. It works due to the change in mutual inductance between the primary and one of the secondary coils (which are wound in series opposition) when a sample is introduced in it, and this causes a signal to be generated across the secondaries [31]. Usually, the frequency and temperature dependence of the complex susceptibility (real and imaginary components can be separated) is studied, which can be used to help differentiate between different types of slow relaxations and derive energy barriers for that relaxation. It is also employed to study the dynamics of the magnetic system [32], and the non linear susceptibilities can be used to identify and distinguish magnetic transitions. A few examples are shown in Fig(1.8).

The magnetic susceptibility, χ, of an isotropic substance is defined as: "the intensity of magnetization acquired by an infinitely thin bar placed lengthwise in a uniform field of unit magnetic force" [33]. From Fig(1.7a), a random M-H curve, it can be seen that the DC susceptibility is defined as (reasonably valid for Linear Media) –

$$\chi = M/H_{dc}$$

Whereas the AC susceptibility –

$$\chi = dM/dH_{ac}$$

(Assuming that the magnetic response is linear in the region of M-H curve probed). In general, the magnetization (M) might be a more complicated function of the magnetic field (H) (taking demagnetization factors into consideration) –

$$M = M_0 + \chi^{(1)}H + \chi^{(2)}H^2 + \chi(3)H^3 + ...$$

Here, $\chi^{(1)}$, $\chi^{(2)}$, and $\chi^{(3)}$ are the first (linear), second and third (non-linear) order susceptibilities. This M can be expanded as a Fourier series (considering only real susceptibility)
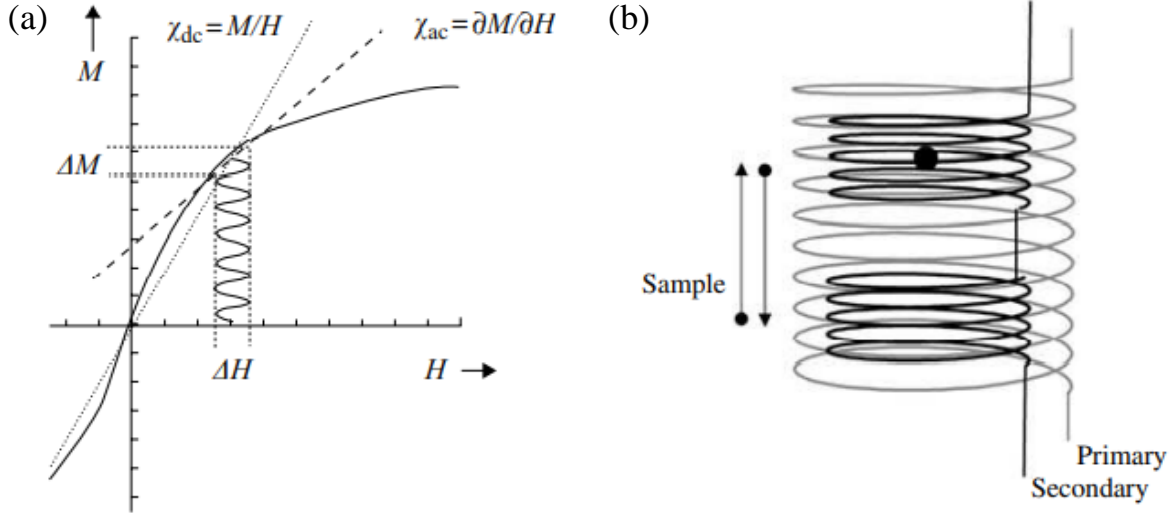
Figure 1.7: (a) M-H curve explaining AC and DC susceptibility [34]. (b) General coil design of an AC susceptometer [34].

[14]–

$$M = M_0 + \sum_{n=1}^{\infty} \mathcal{M}_n \cos(n\omega t)$$

Where –

$$\mathcal{M}_1 = \chi^{(1)} H_{a.c.} + \frac{3}{4}\chi^{(3)} H_{a.c.}^3 + \frac{5}{8}\chi^{(5)} H_{a.c.}^5 + \dots$$

$$\mathcal{M}_2 = \frac{1}{2}\chi^{(2)} H_{a.c.}^2 + \frac{1}{2}\chi^{(4)} H_{a.c.}^4 + \dots \tag{1.4}$$

$$\mathcal{M}_3 = \frac{1}{4}\chi^{(3)} H_{a.c.}^3 + \frac{5}{16}\chi^{(5)} H_{a.c.}^5 + \dots$$

Here, the even non-linear susceptibilities are an indication of an internal symmetry breaking field (inversion symmetry of M w.r.t. H).

The basic setup of an AC susceptometer consists of two secondary coils in series opposition (to cancel the voltages due to AC field of the primary) symmetrically placed inside a primary coil so that the signals produced in the two coils ideally cancel out in the absence of a sample (which they don't in reality due to differences in the wound secondary coils) (see Fig(1.7b)). When a magnetic sample with volume (V) averaged magnetization (M) is placed inside one

of the secondaries, the total flux Φ through the two secondaries is –

$$\Phi = \mu_0 \pi a^2 N((VM(t) + H) - H)$$

Where a is the radius of the secondary with N total loops. Fourier expanding M(t) (each $\chi = \chi' + i\chi''$) –

$$M(t) = \sum_{n=1}^{\infty} h(A' \cos{(n\omega t)} + A'' \sin{(n\omega t)})$$

Here, A' and A'' are just a pre-factor. They are just combinations of some power of 'h' with $\chi'^{(n)}$ or $\chi''^{(n)}$, as can be seen from Eq(1.4) above. Furthermore, because of the relation between cos and sin (any function of $\cos{(n\omega t)}$ has an out of phase function with cos replaced by sin), A' and A'' are also similar, with just $\chi'^{(n)}$ in A' replaced by $\chi''^{(n)}$.
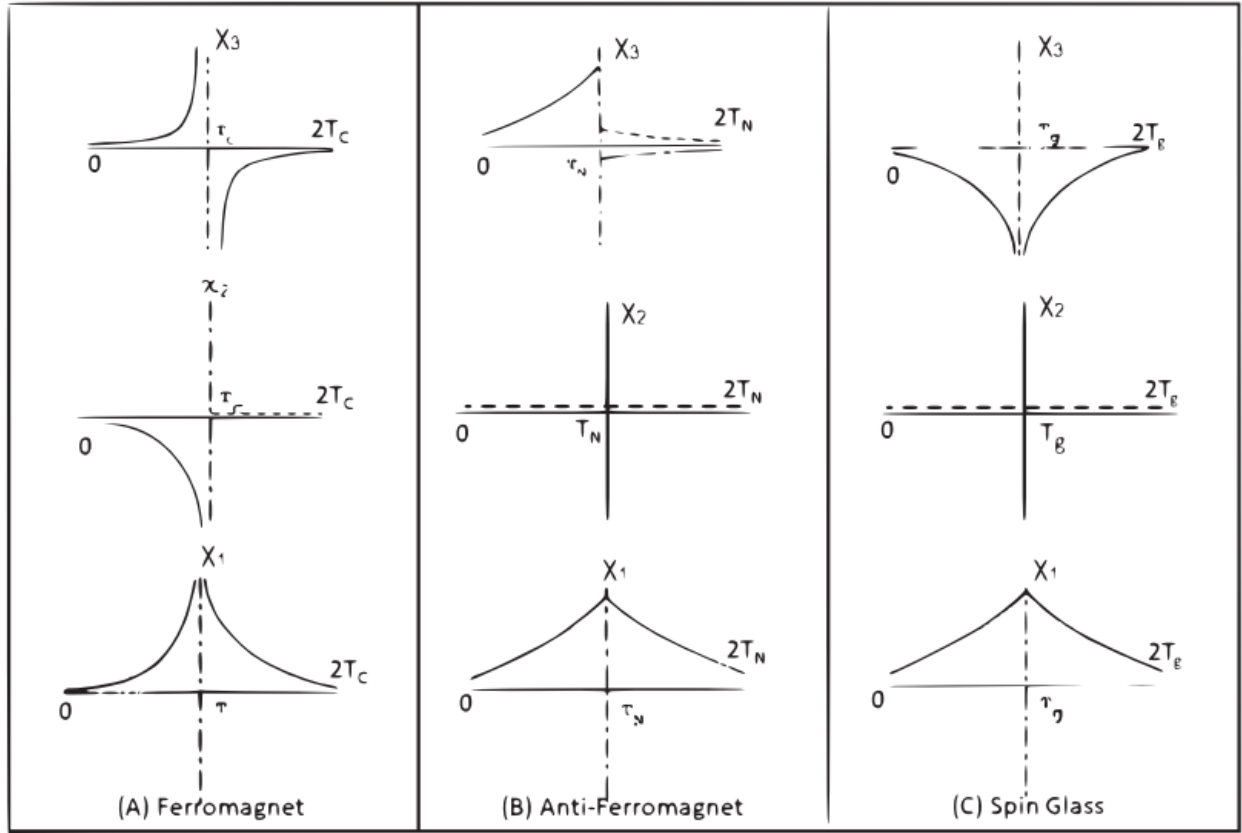
Figure 1.8: Schematic linear and non-linear AC susceptibilities for (a) FM, (b) AFM and (c) Spin Glass [35]

Therefore, $v(t) = -\frac{d\Phi}{dt}$ is [15]–

$$v(t) = \mu_0 \pi a^2 \omega N V h \sum_{n=1}^{\infty} n(A' \sin(n\omega t) - A'' \cos(n\omega t))$$

And we get, for in phase part –

$$|v(t)| = \alpha n_S V \omega \mu_0 h |A'| \tag{1.5}$$

Here, α is the filling factor, n_S is the number of turns per unit length. This is the equation used when calibrating the setup to find the value of the unknown quantity $\alpha n_S \mu_0$, known as the calibration constant.

Using the AC Susceptometer, three main regions defined according to the spin dynamics may be probed [14]. Let τ be the characteristic relaxation time of the magnetic moments of the system.

1. $\omega \ll 1/\tau$: Here, susceptibility obtained ($\chi_{a.c.} \approx \chi_{d.c.}$). The moments have enough time to exchange energy with the lattice, and this is a kind of equilibrium response. The measured susceptibility here is the isothermal susceptibility, χ_T.

2. $\omega \gg 1/\tau$: Here, the moments do not have time to exchange energy with the lattice. The susceptibility measured here is the adiabatic susceptibility, χ_S.

3. $\omega \approx 1/\tau$: Here, the linear response theory predicts a phase lag in the response of moments w.r.t. the applied field. Hence, the response has real (in-phase) and imaginary (out-of-phase) components respectively.

Starting next chapter, the thesis first discusses the magnetization data on powder crystalline samples of NiF_2 and CoF_2 (chapter 2). Chapter 3 then discusses the constructed LHe compatible AC-Susceptometer. The AC-susceptibility data is discussed in chapter 4. Finally, the thesis ends with chapter 5 which provides conclusion and discusses the future prospects.

Chapter 2

Magnetization and Remanent Magnetization on NiF$_2$ & CoF$_2$ Micro - Crystals

2.1 Structure and Properties of NiF$_2$ and CoF$_2$

NiF$_2$ has a rutile type crystal structure (shown in Fig(2.1c)) with orthorhombic distortion [36]. In 1954, Maltarrese and Stout concluded that the ionic spins point along the a or the b-axis in the AFM structure (below 73.3K) by investigating its magnetic anisotropy [37]. The corner ion (0, 0, 0) spins are parallel while the center ion ($\frac{1}{2}$, $\frac{1}{2}$, $\frac{1}{2}$) spins are anti-parallel. This was later confirmed by Shulman [11] who also showed that the spins are canted in the ab-plane (by 0.9°from the a or the b-axis [22]) to give it a weak ferromagnetism perpendicular to these axes. The Néel temperature of NiF$_2$, $T_N \approx 73.3K$, was first accurately determined by Stout and Catalano in 1953 together with CoF$_2$ and FeF$_2$ by measuring their magnetic susceptibilities [38]. Above this temperature, it behaves as a paramagnet, and below it, as a WFM. The space group of NiF$_2$ is $P42/mnm$ (refer to Fig(1(b)) for the symmetry elements). The Ni^{2+} ions are subjected to an orthorhombic crystal field [12], [22], and since fluorine is a weak field ligand, the moment of Ni^{2+} ion is close to the free ion value of $2\mu_B$.

CoF$_2$ also possesses rutile type crystal structure and the same space group as NiF$_2$
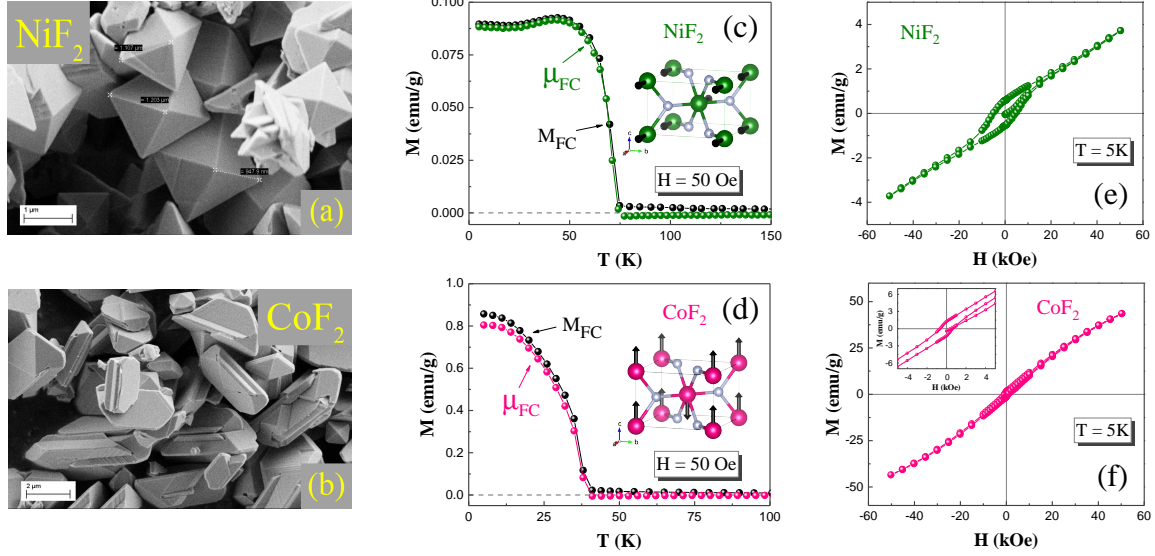
Figure 2.1: SEM images for (a) NiF$_2$ and (b) CoF$_2$.(taken from Sri Pragna Dubbaku's End-Sem project report) Crystal structure [36] and, TRM (μ_{FC}) and Magnetization (M$_{FC}$) as a function of temperature of (c) NiF$_2$ and (d) CoF$_2$ for $H = 50 Oe$. M-H isotherms (field cooled at 100 Oe) for (e) NiF$_2$ and (f) CoF$_2$ (inset – M-H isotherm in lower field region).

($P42/mnm$) (Fig(2.1d)). However, in the absence of an external pressure, the spins in CoF$_2$ point in [001] direction (along c-axis) [27]. Its Néel temperature is $T_N \approx 37.7K$, as determined by Stout and Catalano in 1953 [38]. The spin of free Co^{2+} ion is 1.5, however experiments have shown that it is significantly reduced to ~ 1.107 [26].

2.2 Experimental Technique

The micro-crystals used in this work are synthesized & characterized in our lab by Sri Pragna Dubbaku using solvothermal synthesis technique. The Scanning Electron Microscopy (SEM) images are recorded using Zeiss Ultra Plus field-emission SEM. All the magnetization measurements were carried out using SQUID magnetometer from Quantum Design.

2.2.1 Experimental Protocol

Typically, the magnetization (M) as a function of temperature (T) measurements are carried out using either the Field Cooled (FC) or the Zero Field Cooled (ZFC) protocol. These are important because their comparison can give information about anisotropy, which is relevant to our discussion [39]. The measurements presented here follow the FC protocol. In this, a magnetic field is applied to the sample at a temperature above its transition (at 200K, above the sample's T_N in this case). It is then cooled in presence of the applied field down to 5K below its T_N, and the corresponding M is recorded. The field is then switched off, and the TRM is measured as a function of time or of temperature by heating the sample to above its T_N. The measured M in presence of H is called M_{FC} and the corresponding TRM (measured in zero H) is called μ_{FC}. TRM contains information not present in routine M-H isotherms or M vs T measurements. It has been successfully used to probe the slow spin relaxation is spin glasses, superparamagnets etc. [40], [41]. It appears that this is also significant in probing WFMs as these systems exhibit a unique ultra-slow relaxation with counter-intuitive H dependence [5]–[8].

A representative M_{FC} and μ_{FC} vs T is presented in Fig(2.1c) and Fig(2.1d) for H = 50 Oe. Here we differentiate two aspects. First is the absolute magnitude of TRM for a given H and the second is percentage retention, i.e. what percent of the corresponding M is retained after switching off the H (see Table 2.1 and Table 2.2). The percentage retention is higher in NiF_2, however, the magnitude of TRM is greater for CoF_2. This is a trend we will see at all other fields too and will be discussed in a bit more detail. The TRM above T_N has a very small negative value (also seen at all other fields) when it should ideally be zero. This may apparently arise due to the residual field of the SQUID magnetometer, which is generally of the order of a few Oe [6]. Fig(2.1e) Fig(2.1f) present the M-H isotherms for NiF_2 and CoF_2 respectively. These are taken at 5K for both the samples and were prepared after field cooling at 100 Oe. Both the M-H isotherms show a small opening of the loop along with non-saturating behaviour at higher H, which typically shows the presence of weak ferromagnetism. They are also non-saturating, even for fields as high as 50 kOe, indicating the anti-ferromagnetic nature of the samples. These results are discussed in more details in the following section.

H (Oe)	M_{FC} (emu/g)	μ_{FC} (emu/g)	% Retention
50	0.090	0.088	97.8
500	0.252	0.232	92.1
1 k	0.370	0.321	86.8
3 k	0.689	0.500	72.6
5 k	0.871	0.551	63.3
10 k	1.214	0.585	48.2

Table 2.1: Magnetization (M_{FC}), TRM (μ_{FC}), and % of M retained as TRM @ T = 5K, at various cooling fields (H) for NiF_2.

H (Oe)	M_{FC} (emu/g)	μ_{FC} (emu/g)	% Retention
50	0.857	0.804	93.8
500	1.722	1.190	69.1
1 k	2.342	1.273	54.3
3 k	4.565	1.394	30.5
5 k	6.675	1.442	21.6
10 k	11.808	1.494	12.6

Table 2.2: Magnetization (M_{FC}), TRM (μ_{FC}), and % of M retained as TRM @ T = 5K, at various cooling fields (H) for CoF_2.

2.3 Results and Discussion

2.3.1 M-H Isotherms

Fig(2.1e) shows M-H isotherm recorded at 5K for NiF_2 micro-crystals. The morphology of the crystals is shown in Fig(2.1a). The M-H isotherm shows a small opening in fields up to 10 kOe, followed by a non-saturating behaviour at H > 10 KOe. It is linear with almost equal slopes for increasing and decreasing field after about 10 kOe – 15 kOe. This is significantly different from what is seen for a SC. The linearity in M-H curve starts at $\approx$ 5 kOe for a SC when field is applied parallel to the a or b axis [22], [42]. The anisotropy in the ab-plane is high for NiF_2, unlike the DMI driven WFMs [12]. This causes the direction of moment to not coincide with the applied field when it is not along the a or the b axis, except at high fields [12]. This can also be seen from the M vs H plot by Bazhan et al. [27] where the linearity started at H $\approx$ 20 kOe when the field was applied parallel to [110]. In a powder sample similar to ours in which the micro-crystals are oriented in all random directions (Fig(2.1)), the coercivities are found as $Hc_1 \approx$ -5.2 kOe, $Hc_2 \approx$ 4.6 kOe respectively. It is to be noted

that the MH isotherm (at 5K) has been recorded in the field cooled state. Here sample is first cooled in presence of 100 Oe down to 5K. Prior to recording the MH isotherm, the field has been switched off.

For CoF_2, M-H isotherm is obtained under similar condition (FC at 100 Oe). The coercivity obtained is $Hc_1 \approx$ -0.65 kOe, $Hc_2 \approx$ 0.63 kOe. Hence we note that the difference in coercivities (Hc_1 and Hc_2) is significantly larger for NiF_2. The linearity in M-H isotherm starts at field $\approx$ 2 kOe. The case of CoF_2 is an interesting one. CoF_2 has its spins pointing along the c-axis [27], and is an AFM in the absence of an external pressure according to Moriya, Borovik-Romanov, and others (a small WFM moment is indeed seen, but it is negligible in comparison to the PzM moments observed) [10], [12], [43]. It is a PzM and develops a magnetic moment when external pressure is applied to it. This moment may either be due to canting of the spins or inequivalence of the sublattice magnetizations, the direction of pressure determining the type [10], [44]. This along with the fact that these are micron sized crystallites would imply that no opening of the loop associated with strain due to nano-scaling should be observed in the CoF_2 sample. There can however be magnetoelastic anisotropy effects related to defects (anisotropy due to mechanical stresses in a magnetic material [45]). Unlike a regular AFM, the longitudinal susceptibility (parallel to c-axis) of CoF_2 does not tend to zero as T approaches 0 K [46], [47]. Köbler et al. also argue that there would be spins pointing in all three directions on the basis of the temperature dependence of its spontaneous magnetization[48]. Fuerthermore, there is also a lack of magnetization and susceptibility data on CoF_2 SC. However, since CoF_2 is a PzM, then given the remanence magnetization in the M-H isotherms, we can try to find what the strain in a CoF_2 SC would be for it to produce a magnetization equivalent to the one seen in these micro-crystals. In the paper by Borovik-Romanov, he applied pressure ($p = 2\sigma$) along the bisector of x and z axes (spins point along the z-axis), to produce canting of the spins and a moment along y-axis. The relation between stress (σ_{xz} in kg/cm2) and the spontaneous moment (M_S in emu/mole) is [10] –

$$M_S = 5.1x10 - 2 \cdot \sigma_{xz}$$

Putting here, the value of $M_S \approx$ 121.7 emu/mole from the M-H isotherm of CoF_2, one gets $\sigma_{xz} \approx$ 2386.3 kg/cm^2. Hence, the crystallites of CoF_2 are behaving equivalent to a SC having pressure, $p = 2\sigma \approx$ 4750 kg/cm^2 at 20.4 K temperature which is pretty large.
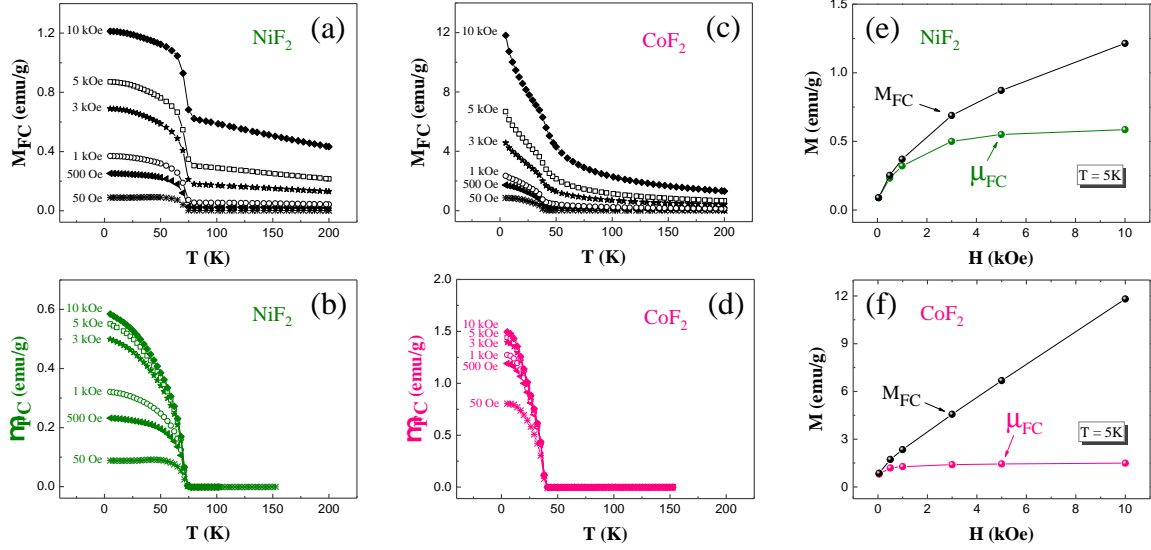
Figure 2.2: Magnetization as a function of Temperature for (a) NiF_2 and (c) CoF_2, and TRM as a function of Temperature for (b) NiF_2 and (d) CoF_2 for various cooling fields. TRM and Magnetization as a function of cooling field for (e) NiF_2 and (f) CoF_2

2.3.2 Magnetization and TRM Measurements

The M vs T plots are given in Fig(2.2a) for NiF_2 and Fig(2.2c) for CoF_2. It is easy to see that these are similar to the ones obtained for the DMI driven WFMs [5], [7], [8]. The M vs T plot obtained for CoF_2 is again unexpected (just like the loop opening in M-H isotherm). The magnetization appears to be consistent with weak ferromagnetism. Here, T_N can be picked from M vs T plots, however, it is easier to see it in the μ_{FC} vs T plots as the remanence goes to zero in the paramagnetic region.

Comparing the M vs T curves of NiF_2 and CoF_2, it can be seen instantly that the magnetization in CoF_2 is an order of magnitude greater than that in NiF_2. It is to be noted that the T_N (CoF_2) < T_N (NiF_2). It has been observed in the DMI driven WFMs that the samples with higher magnetization (and corresponding TRM) at a particular field had lower T_N [7], [8]. This is due to the fact that DMI driven systems depend more on J (exchange coefficient) and hence the transition temperature. Though fluorides are primarily SIA driven, yet we observe that both magnetization and remanence are correspondingly larger in samples with lower T_N.

We also note that the temperature dependence of magnetization for CoF_2 (unlike that of

30

NiF$_2$) does not appear like that of a typical WFM. NiF$_2$ shows a more saturating magnetization behavior as temperature approaches 0 K. CoF$_2$, on the other hand, shows an increasing slope. Hence, it appears that the μ_{FC} vs T instead of M$_{FC}$ vs T brings out the role that spin canting plays here. In NiF$_2$, since the plot is similar to that of a WFM, the increasing magnetization may be arising mainly due to moments flipping towards the field direction as temperature decreases. In CoF$_2$ however, there might also be a contribution of the difference between sublattice magnetizations [49].

The μ_{FC} vs T is also shown in Fig(2.2b) and Fig(2.2d). The first thing noticed here is that the TRM is almost zero in the paramagnetic region. Hence, the T$_N$ for both the samples can be sharply located as compared to what one finds from M vs T data; T$_N$ (NiF$_2$) = 74 ± 2 K, T$_N$ (CoF$_2$) = 41 ± 2 K, and these values agree with literature [37], [38]. The μ_{FC} vs T for both NiF$_2$ and CoF$_2$ seems to be qualitatively similar. We also note that the TRM retained is higher for NiF$_2$, even though its magnetization and remanence is lower. The reason for this appears to be the relatively quicker saturation of CoF$_2$ remanence. In order to bring forward these features more clearly, we have compared M vs H and μ_{FC} vs H for both the samples.

The M vs H data is picked from the M vs T plot at T = 5K. Similarly, for the μ_{FC} vs H it is picked from the μ_{FC} vs T plot. While the M vs H is non-saturating in both the samples, the μ_{FC} vs H shows saturating trends. The TRM for CoF$_2$ also shows the tendency for a faster rise when compared to NiF$_2$. Here we emphasize that remanence shows FM like behaviour for both the samples and the field dependence of remanence is strikingly different from DMI driven WFMs. Unlike the DMI driven WFMs, the TRM in both of these does not show a characteristic peak-like feature with increasing cooling field (atleast for fields till 10 kOe) [5]–[8]. The reason behind this observation is not very clear at this moment. However, a probable explanation can be related to the domain wall energy of SIA driven WFMs. For instance, the domain wall energy in case of NiF$_2$ is estimated to be around 0.2 ergs/cm^2, which is significantly more than the DMI driven WFMs, wherein rotation of the spins in the basal plane would be easier [12]. The relaxation energy released would then easily be able to flip the domains at lower cooling fields in DMI driven WFMs, while this would require much higher fields for SIA driven WFMs.

The ultra-slow relaxation, along with the counter-intuitive H-dependence of TRM could be taken as foot print of spin canting in DMI driven system [5]–[8]. It remains to be seen,

31
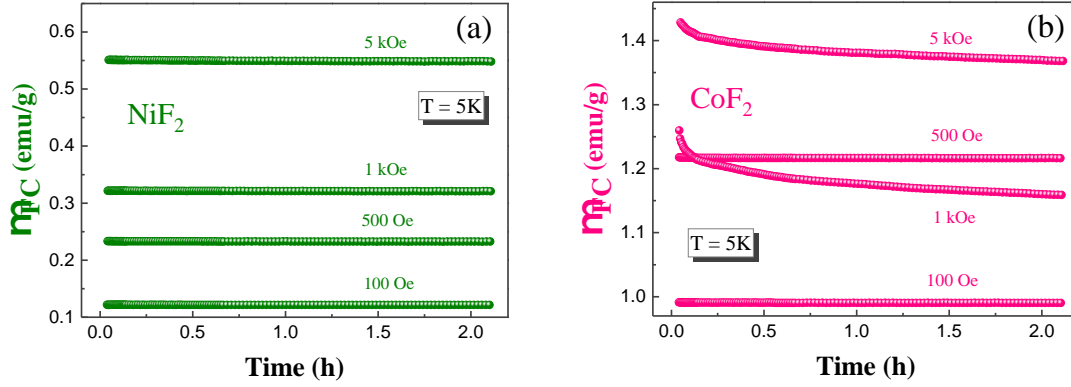
Figure 2.3: Remanence as a function of time for (a) NiF_2 and (b) CoF_2.

especially from the field dependence data in SC of both these fluorides, whether the H dependence of TRM enables us to differentiate between the DMI and the SIA driven spin-canting. As mentioned earlier, the time stable remanence (similar to DMI driven systems) is seen in both CoF_2 and NiF_2 and is discussed in the next section.

2.3.3 Time-stable remanence

TRM as a function of Time is shown at T = 5K for CoF_2 and NiF_2 in Fig(2.3a) and Fig(2.3b) respectively. These data are recorded at various cooling fields. Similar to what is observed for the DMI driven systems, both samples show a quasi-static remanence and the remanence is more stable for sample with higher T_N [5]–[8]. An intriguing observation is the significant drop in TRM retention for CoF_2 after a particular field (Fig(2.3b)). Therefore, it seems that there are multiple time scales involved in this relaxation which need to be looked into further. It appears that CoF_2 also shows tendency for a counter-intuitive field dependence at cooling fields below 1 kOe. However, more data is needed to further confirm this. It is to be noted that similar observation was earlier reported by Borovik-Romanov (1960) albeit in a different context [10]. He found that when the field direction is reversed in a CoF_2 SC, the magnetization also tends to rotate towards that direction. This happens after a particular threshold field (depends on the stress in the crystal) and occurs slowly in 5-7 minutes. This observation seems to be connected to our remanence data on CoF_2. It should also be noted here that the NiF_2 and CoF_2 crystallites are not nano-scaled and they are not even a glassy system, which can show such relaxation dynamics [50], [51]. In the next

Figure 2.4: Field-cooled DC susceptibility as a function of temperature for (a) NiF_2 and (b) CoF_2 for various cooling fields.

sub-section, we present field dependent M vs T data for both the samples. This is important because for SIA driven WFMs including CoF_2 and NiF_2, anomalies have been reported in the paramagnetic region [24], [48].

2.3.4 Susceptibility Measurements and Non-Linearity in Paramagnetic Region

The susceptibility data is obtained from the magnetization vs temperature data by dividing it with the field applied (Fig(2.4)) (emu/mol) and its inverse is also plotted (Fig(2.5)) in the paramagnetic region. As derived theoretically by Moriya, and also seen experimentally by Cooke et al[24], [52], the susceptibility of NiF_2 ceases to follow the Curie-Weiss law below 120 K (which is about the same temperature as seen in our curves Fig(2.5)). This is due to SIA and different easy axes of different ions in the lattice (hence they have different Curie constants when field is aplied along the easy axis of any one ion). As stated by Cooke et al, the susceptibility increases much more slowly below 120 K before finally increasing much more rapidly at temperatures close to T_N. This is precisely what is seen here. However, this effect is only seen at lower fields and not at fields above 3 kOe, where it appears that the Zeeman energy might be dominant enough that the SIA can be neglected. One thing to note here is that the susceptibility values obtained are a little less than what is obtained by Cooke et al ($\approx$ 0.005 emu/mol as compared to $\approx$ 0.007 emu/mol), however as stated

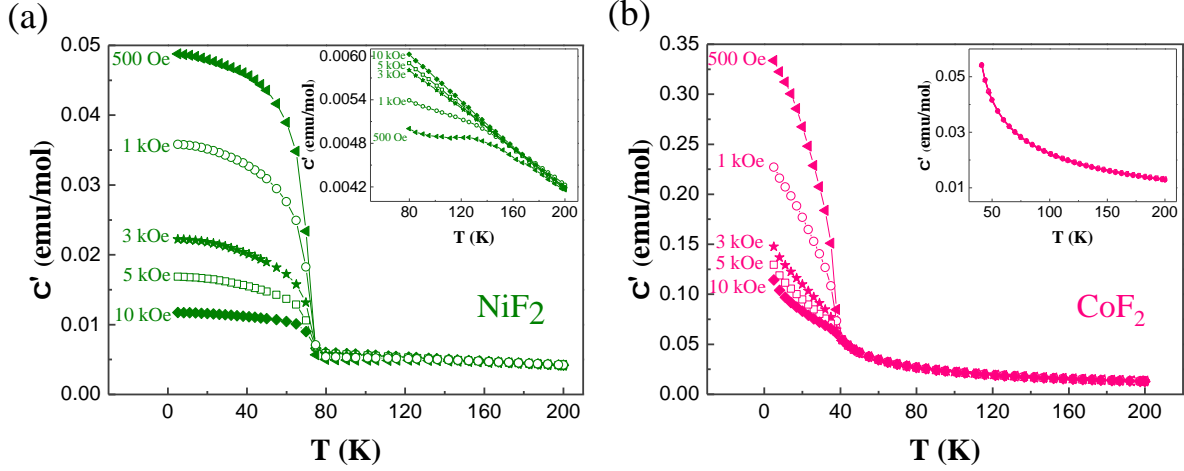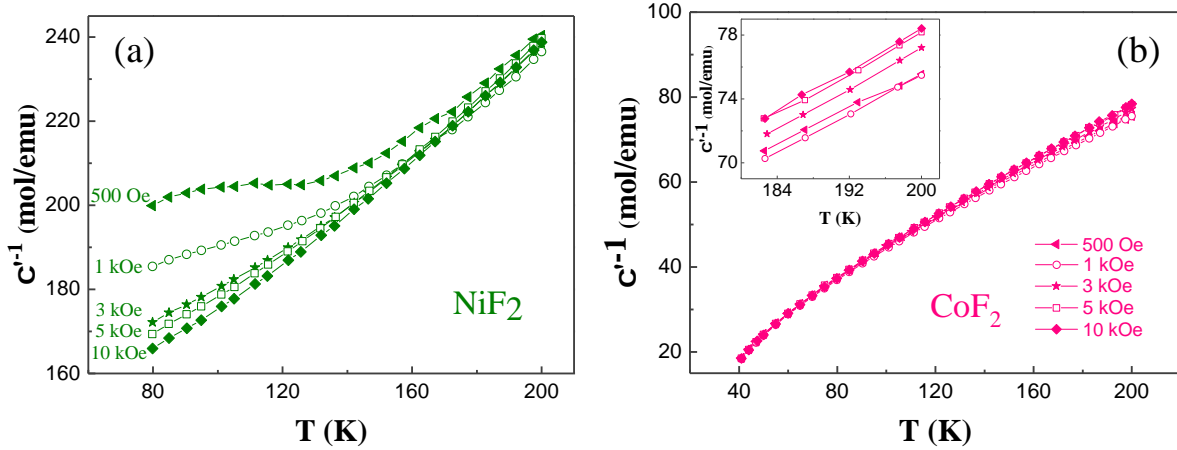**Figure 2.5:** Inverse of Field-cooled DC susceptibility as a function of temperature for (a) NiF_2 and (b) CoF_2 for various cooling fields.

by them, their susceptibility measurements are not that accurate. The more interesting observation is the lack of such an effect in CoF_2. While both samples show anomaly in the paramagnetic region, the effect is significantly pronounced for NiF_2 as compared to CoF_2.

The anomalies in the paramagnetic region can be seen more clearly when inverse susceptibility is plotted above the magnetic transition. Typically short range correlations lead to deviations from the Curie-Weiss law in the vicinity of the magnetic transition. However what we observe here is that these anomalies in the paramagnetic region exist much above the magnetic transition. This is presented in Fig(2.5), where inverse susceptibility is shown in the paramagnetic region. As is evident from these data, deviation from the Curie-Weiss law is seen for both NiF_2 and CoF_2 samples. From the linear region of the data, the values of Curie constants are obtained to be 1.58 emu.k/mol for 3 kOe and 1.50 emu.k/mol for 10 kOe field for NiF_2. The average error was around 0.02, due to the 95% confidence interval of the fitting. These values are reasonably close to the value of Curie constant of 1.36 emu.k/mol obtained by Cooke [24].

The CoF_2 curve also shows non-linearity below ~ 80 K. These features may be related to the reduction of the spin angular momentum due to crystal field effects as described by Köbler *et al* [48]. A rigorous theoretical treatment by Nakamura and Taketa [49] presents this as a result of the difference in magnetic moments of the body center and the corner ions below a particular temperature. We can also compare this to DC susceptibility measurement

by Astrov *et al.* [43]. Astrov obtained a Curie Constant, C = 2.72 emu.K/mol and Curie temperature, θ = -50K. Our micro-crystalline sample has C $\approx$ 3.09 emu.K/mol and $\theta \approx$ -42.5K (in the linear region, for H = 500 Oe).

Based on the observations in the present chapter, it appears that the technique of AC-Susceptibility would be suitable to probe the quasi-static remanence in these SIA driven WFMs. In the next chapter we will look at the fabrication of a LHe compatible AC-Susceptometer for probing the SCs of these WFMs.

Chapter 3

Fabrication of the LHe compatible AC-Susceptometer

The AC-Susceptometer consists of a primary coil and a pair of secondary coils, which are wound in series opposition. Typically a separate coil former for both AC and DC coils hangs outside the low temperature insert [53], [54]. In our case, the secondary coils are wound directly on quartz glass tubes, which is already a part of low temperature insert. This should lead to a significant enhancement in the sensitivity of the AC bridge. To the best of our knowledge, such a design has not been reported in literature. In addition to this, a low temperature insert compatible with LHe temperature has been designed and fabricated during the course of this project. This is particularly relevant as we are exploring both linear and non-linear susceptibility in AFMs and WFMs, systems which produce significantly lower magnetic signal as compared to a routine FM. Due to lack of time, we could calibrate our setup down to LN_2 temperature, though the setup is ready for LHe measurements. The details of design, fabrication and calibration of this sensitive susceptometer are presented in this chapter.

3.1 Design of the Liquid Helium Compatible Insert
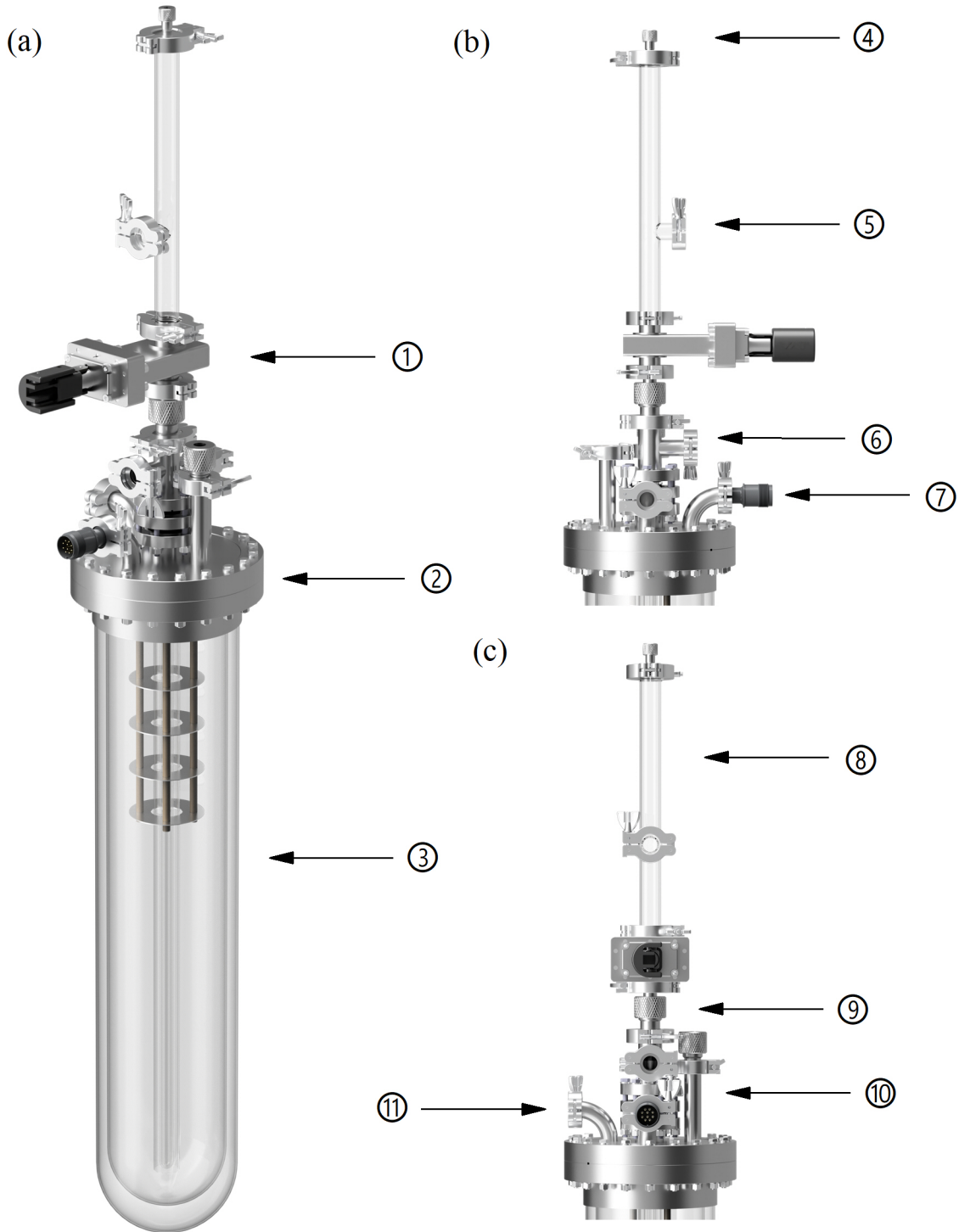
Figure 3.1: CAD design of AC-Susceptometer (designed in Fusion 360, labels in text) (a) Full View (b) Front View (c) Side View

The setup consists of a cluster flange which is a modified Cf-150 flange (②), which holds the primary and secondary coils (Fig(3.1)). This is connected to a LHe Dewar ((③), sealed to a Cf-150 half nipple using torr seal). Above the cluster flange is a Kf-25 adapter with glass sealing flange on one side and a Kf-16 Tee connection for vacuuming the inter-space (⑥). This is connected to a glass tube (with glass to metal seal) using a Kf-25 flange (⑨). A light weight Aluminium Kf-25 gate valve rests on top of this, which is closed to retain vacuum while removing the sample rod (①). The length of the Kf-25 Tee above the gate valve (300 mm) is chosen such that the sample holder can be easily taken out of the gate valve before closing it (⑧). This also contains a Kf-16 flange for vacuuming the inner space (⑤). Finally, the sample rod is inserted into the setup through a Kf-25 compression port at the top (④). Design of the LHe AC-susceptometer setup is made in Fusion-360 software by Autodesk (Fig(3.1)). This insert was manufactured using non-magnetic (austensitic) stainless steel (SS) 316, though the metallic part showed magnetic signals after thermal cycling [55]. However, these are reasonably far from the coil setup and hence we could achieve a good calibration.

3.1.1 LHe Dewar

The design of the LHe Dewar consists of two borosilicate glass tubes – used because it is much less permeable to He molecules than quartz – having ODs 130 mm and 150 mm, thickness of 3 mm and length 750 mm [56]. The individual glass tubes could be attached separately to the Cf-150 half nipple using Agilent torr seal. The space between the concentric glass tubes can be evacuated using a rotary vane pump using a Kf-26 flange attached to the Cf-150 flange. This is important as He permeates through the borosilicate tubes (albeit very slowly) and can make the vacuum 'soft' if not evacuated continuously [57]. This Dewar setup is placed in another silvered outer Dewar in which LN_2 is filled, so as to minimize LHe evaporation. It is to be noted that a silvered Dewar is needed for LHe measurements which will be procured later.

3.1.2 Cluster Flange

Above the glass Dewar flange sits a modified Cf-150 cluster flange (Fig(3.2b)). This has a center glass flange where a Kf-25 quartz tube (primary coil) sits. This tube is supported
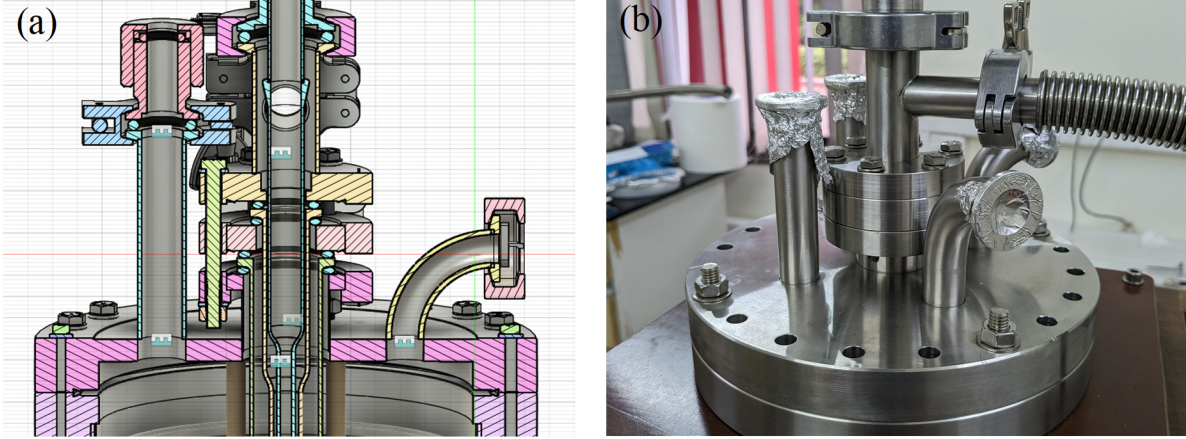
Figure 3.2: (a) Setup to hold primary coil and secondary coil glass tubes between two o-rings (b) Cluster flange.

by two viton o-rings, one on top and another on the bottom which are compressed to form vacuum tight set-up on both sides of the tube (so that He does not escape) (Fig(3.2a)). This compression is obtained by tightening another flange which sits on top of this glass flange and accommodates Kf-16 quartz tube (secondary coil) in a similar manner. Thus, the two quartz tubes are tightened between three SS316 flanges.

The cluster flange also houses four separate out-ports around he center glass flange. One of these is the He out port connected to the He recovery line (⑪), while the other one is the vacuum feedthrough port (⑦), which makes it possible to take out the coil wires from inside the He Dewar while maintaining leakproof configuration. The straight Kf-16 houses a compression port through which one end of the LHe line goes into the setup (⑩). The other end is inside LHe Dewar through which LHe is filled in the setup. The fourth port is additional and is closed with a blind for future use.

3.2   Coil Winding

3.2.1   Primary Coil

The primary coil is wound on a quartz tube of Outer Diameter (OD) 28 mm and Inner Diameter (ID) 25 mm (Fig(3.3a)). This size is chosen so that the secondary coil which has a
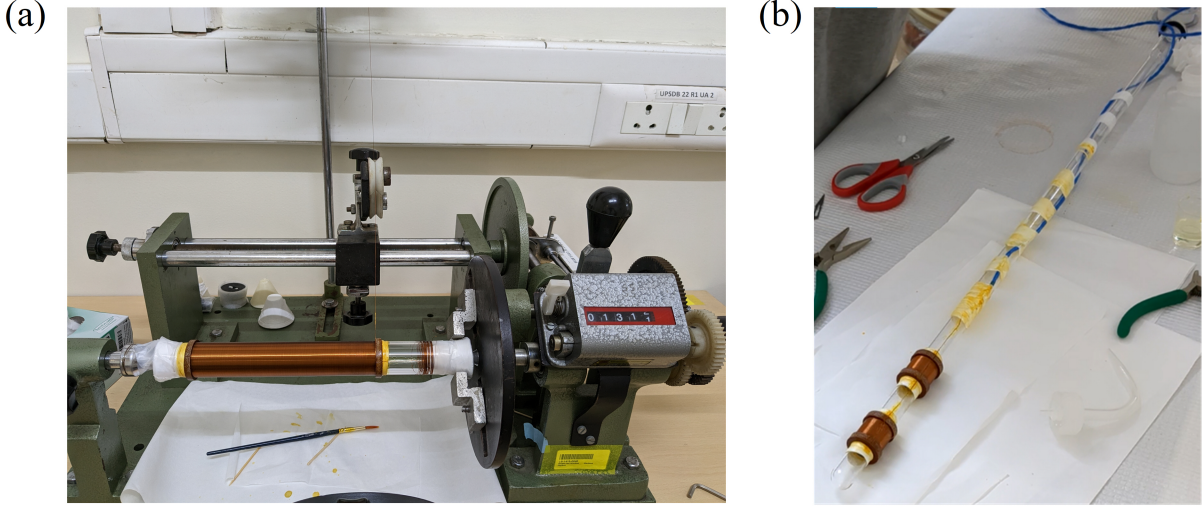
Figure 3.3: (a) Primary coil being wound using linear coil winding machine. (b) Secondary coil

maximum OD 23 mm can easily be accommodated inside the primary. The length of the coil is 150 mm and it is wound using a 36 SWG (0.193 mm diameter) copper wire. It consists of four layers of winding, each layer having either 655 or 656 turns, for a total of 2622 turns. These layers are supported at the ends using hylam rings of appropriate diameter to avoid stress on the quartz tube due to contraction on cooling. The coil was wound using a manual linear coil winding machine following orthocyclic winding(Fig(3.3a)). This type of winding ensures the maximum fill factor (90.7% for round wires) as the wires of the upper layer sit in the grooves of the bottom layer. Orthocyclic winding is one of the most arduous winding scheme to manufacture [58]. The coil is then fused to another quartz tube which has a quartz Kf-25 flange fused to its top end. The length of this whole setup is about 700 mm. A 3-4 mm diameter hole is also made in the primary quartz tube below the flange to take out wires from the secondary coil. The resistance of the primary coil is 139 Ω at room temperature and 16.9 Ω in LN$_2$.

3.2.2 Secondary Coil

The quartz tube on which the secondary coils are wound has an OD of 15 mm and an ID of 12 mm, such that another quartz tube of OD 10 mm can safely go inside it (Fig(3.3b)). A nonmetallic and non magnetic former is desired for ac chi, and typically Hylam former is

used for such purpose [53], [54]. This former typically hangs outside the low temperature insert and the distance of the sample from the secondary former should be as low as possible. The upper limit is set by the OD of the low temperature insert which needs to fit inside the secondary former. In our case the coil is wound on the outer tube of the low temperature insert itself. This has significantly improved the filling ratio[59].

The coils have a length of 15 mm and are separated by a distance of 50 mm. This is chosen so that the coils are in a region of constant magnetic field inside the primary and the flux coupling between the secondary coils can be minimised, optimizing the fill factor. The secondary is wound using a 42 SWG (0.1016 mm diameter) copper wire and consists of 3494 turns on one coil and 3523 on the other to compensate for the coil offset. Here too, orthocyclic winding was used, and it was later fused to another quartz tube with Kf-16 flange on top. The length is taken such that the center of the primary coil coincides with the mid point of the secondaries when they are assembled in the setup. The resistance of the secondary coil is 859 Ω at room temperature and 106 Ω in LN$_2$. Winding the secondary on the glass tube itself instead of a separate hylam former has led to an increase in sensitivity of the setup by about 1.6 times. This comparison is between the present setup (compatible with LHe) and the already existing setup (down to LN$_2$) which contains a Hylam coil former. It is to be emphasized that the length of the primary and the secondary as well as the number of turns in the secondary (pickup coils) is similar in both cases. This enhancement of 1.6 times is significant, especially if AFMs are to be probed using the technique of AC-susceptibility is setup with high number of turns ($\sim$ 3000 each coil), such as reported in our work as compared to that discussed in this reference [53], [54]. While there are reports of winding a few turns on the sample itself, but such bridges are suitable for high frequency/ low sensitivity measurements for tracking a magnetic transition. However detecting linear and non-linear AC-susceptibility in AFM remains a challenge and our work paves a way to explore functional AFM using the versatile technique of ac-chi.

Both the primary and the secondary coils are connected to the feedthrough port by Lakeshore CC-SC-50 cryogenic coaxial cable. Outside the LHe Dewar, two high quality twinaxial shielded wires are used to connect the coils to the lock-in amplifier.
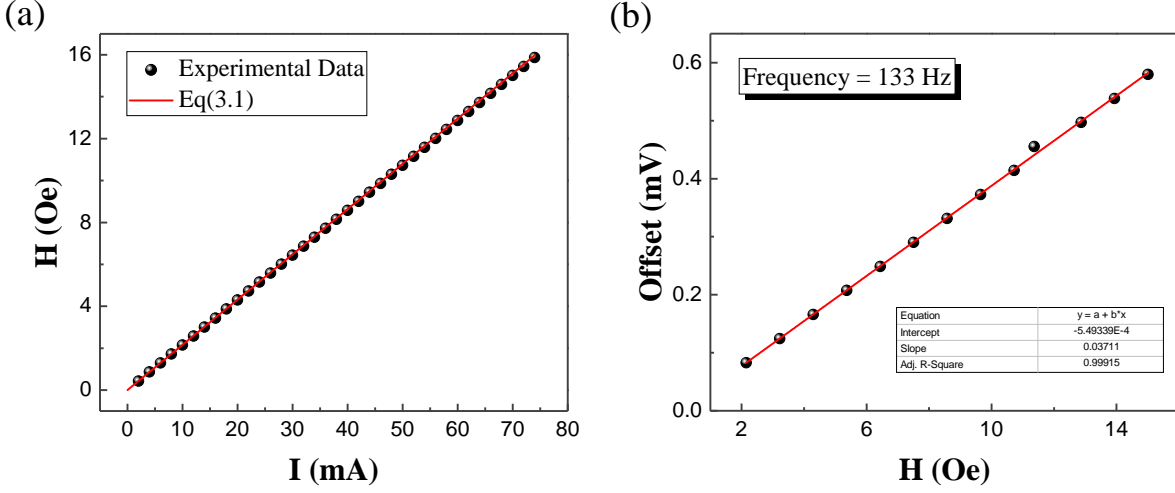
Figure 3.4: (a) Field at the center of the primary coil as a function of current passed through it. (b) Offset in the Secondary coils as a function of Field of the primary.

3.2.3 Coil Characterization and Removing the Offset

To characterize the primary coil, field produced at the center of the coil as a function of current passed through it (both AC and DC) was taken using Lakeshore Model 475 DSP Gaussmeter (Fig(3.4a)) using an axial gauss probe. The theoretical curve (Eq(3.1)) is also plotted in the same graph and matches the experimental result astoundingly well. The field produced by the primary, H, along its central axis is given by –

$$H = \frac{1}{2}\mu_0 nI\left(\frac{y + L/2}{\sqrt{(y + L/2)^2 + R^2}} - \frac{y - L/2}{\sqrt{(y - L/2)^2 + R^2}}\right) \tag{3.1}$$

Where n is the number of turns per unit length, I is the current in the coil, L is the coil length, R is its radius, and y is the distance from the center of the coil.

The offset of the secondary coil was also removed, both at room temperature and at 77K (LN$_2$ temperature), so that small signals from samples can be detected as the sensitivity of the lock-in amplifier could then be increased. This was done by assembling the setup and checking the offset after removing turns from the bottom secondary coil in steps of 10 turns at a time. Each time the two coils were de-soldered and soldered again after removing the turns. The final offset of 369.5 μV was obtained after removing 159 turns from one coil and 32 turns from the other. This offset is sufficiently less for taking measurements on our

Figure 3.5: Sample Rod with redone elements

samples.

After this, the offset dependence on field of the primary coil was also investigated (Fig(3.4b)). From Eq(1.5), it can be seen that it should depend linearly on the field and this is also seen in the figure. The linearity of the bridge with respect to frequency is yet to be checked. Considering the dimensions of the primary and the secondary, and the number of turns in the secondary, it is expected that our bridge is suitable for low frequency measurements below 3 kHz.

3.3   Sample Rod Construction

The sample rod of the existing setup (down to LN_2) is also compatible with the new setup. However, few modifications were made in the existing sample rod (Fig(3.5)). We first discuss the design of the existing sample rod which consists of three different materials. This includes the Sapphire sample holder, a non-magnetic hylam rod which is further connected to a thin-walled SS tube (non-magnetic). Sapphire is the material of choice for holding the sample due to its excellent thermal conductivity [60] and bad electrical conductivity (insulator). This is supported by a hylam (bakelite) rod which is used because it is a non-magnetic material and can survive cryogenic temperatures. The length of this is chosen to be 22 cm, which is enough to keep the SS rod sufficiently out of the primary coil even when the sample is in the bottom secondary. The top part is a non-magnetic hollow SS rod. It houses all the wires inside and passes through a compression seal at the top of the setup to create vacuum at the sample inner space. The wires taken from the Platinum Resistance Thermometer (PRT) and heater are all twisted together in appropriate pairs throughout the sample rod's length to create a non-inductive coupling.
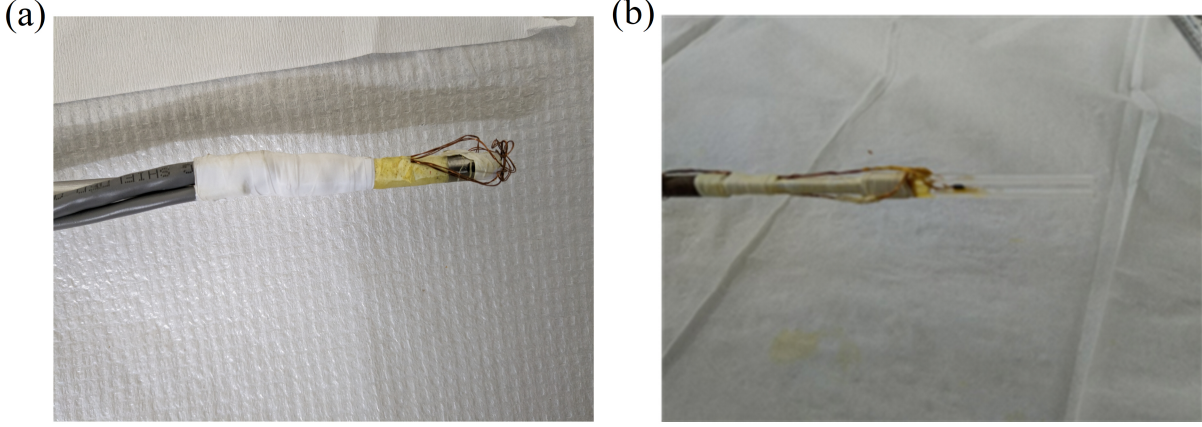
Figure 3.6: (a) Redone connections at the top. (b) New sample holder.

Since the connections (for the heater wire and the PRT) at the top of the sample rod had become lose, they all had to be opened, resoldered again, and carefully secured using teflon (Fig(3.6a)). The new sample holder (Fig(3.6b)) incorporates adding two sapphire SC plates (length 5 cm, width 5 mm and thickness 2 mm) on either sides of a polycrystalline sapphire plate, which is attached to the hylam rod. The entire assembly is fixed using GE 7031 varnish. The sample can be held securely between two sapphire plates. This enables the sample in the center of the coil and accommodates the longer phosphor-bronze heater wire, which is non-magnetic. In the existing sample rod manganin wire was used, which is now replaced with phosphor bronze. The PRT (Innovative Sensor Technology P0K1.232.4SW.B.010) is placed on one of the sapphire SC (which is in contact with the sample) using GE 7031 varnish, and the temperature is read off from lakeshore 336 PID Temperature Controller. This instrument is also connected to the heater wire wound non-inductively on the sample holder, and provides it the necessary power for heating the sample. The PRT is also calibrated using SoftCal Lakeshore software calibration, to read the temperatures more accurately.

3.4   Working of the AC-Susceptometer

The basic principles of the working of an AC susceptometer have already been discussed in chapter 1. Here, the primary coil is connected between the 'signal output (+V and -V)' of the Zurich Instruments MFLI Lock-In amplifier. This provides a sinusoidal voltage output

of a particular frequency (so that it is not a multiple of the line frequency) and amplitude. The secondary coils are connected between the 'Signal Input (+V and -V)' of the Lock-In, and the input is read on a computer connected to the instrument (Fig(3.7a)). This input is measured by the phase sensitive detectors in the lock-in. The real and imaginary parts of the susceptibility are resolved on the lock-in amplifier by setting the reference in phase with the field produced in the primary coil. This is done by setting the reference signal in phase with the voltage across a 1Ω resistor, which is connected in series with the primary coil. This works because the magnetic field in primary coil –

$$H_{primary} \propto I_{circuit}$$

And for a resistor –

$$I_{circuit} \propto V_{resistor}$$

So, for a sample with magnetization M_{sample}, the component in-phase with $H_{primary}$ would produce a voltage across the secondary, $v(t)$, which is $\pi/2$ out-of-phase with $H_{primary}$ ($v(t) = -\frac{d\Phi}{dt}$). The converse can be said about the component of M_{sample} which is out-of-phase with $H_{primary}$. Therefore, the real part of the susceptibility can now be read off as the 'y' component, and imaginary part as the 'x' component of the signal input in the Lock-in amplifier. The higher order susceptibilities are detected simply by measuring the signal across the secondaries at multiples of the primary coil frequency (as can be seen from Eq(1.4)). After every run, a dry run is also taken to subtract the contribution of the coil offset, or other sample rod components (heater wire, PRT etc.) from the sample measurements. This is done by taking measurements without any sample, but with the sample rod at the same position – as it was with the sample – inside the secondary.

3.5 Major Points about the AC-Susceptibility Setup

1. Appropriate connections (as detailed in last section) of the secondary and the primary coils to the lock-in amplifier are made. Similarly, the heater and the temperature sensor (Cernox CX-1030-SD or PRT P0K1.232.4SW.B.010) are connected to the Lakeshore 336 PID Temperature controller. The shields of all these wires are connected to the chassis ground of the respective instruments (star connection is made Fig(3.7a)).

2. The general settings of the Lock-in amplifier (such as bandwidth and roll-off of the low-
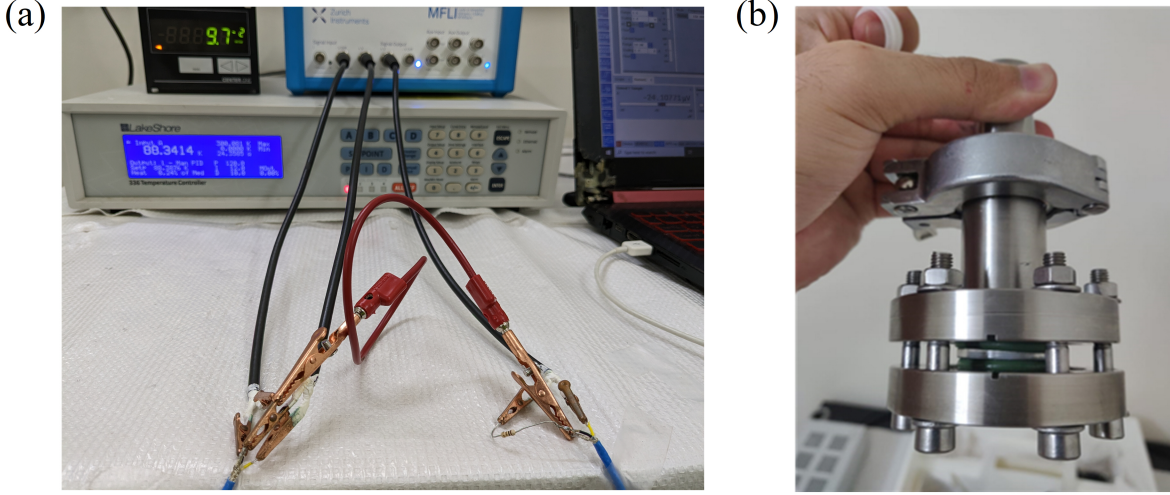
Figure 3.7: (a) Connections to the Lock-in for measurements. (b) sandwiching glass tube between two o-rings for vaccum.

pass filter, the dynamic reserve, type of coupling, etc.) should be kept same as they were while calibrating the setup. This is because these can change the signal values, especially if there is significant noise present around the frequency being probed.

3. The setup has three vacuum channels provided from a single rotary vane pump. One channel evacuates the inter-space (between the secondary coil and the inner glass tube). Another channel evacuates the inner-space (inside the inner glass tube) through a kf-16 flange in the Kf-25 Tee above the gate valve. Both these have ball valves which can be opened for vacuuming and closed while putting in the helium gas for cooling the sample quickly. The inner-space is evacuated during measurements while helium is kept in the inter-space (10^{-1} mbar) for better temperature control. The third channel is for evacuating the space between glass tubes in the LHe Dewar. Since Helium can diffuse through borosilicate glass, this continuous evacuation is necessary to maintain a vacuum jacket. [57].

4. The instrument allows to measure both real and imaginary AC susceptibilities of various orders as a function of temperature, frequency, or field, keeping the other two constant. DC field can also be applied in the same primary coil and AC field can be superimposed over it. This is especially useful to probe weak ferromagnetic which have shown a counter-intuitive remanence profile.[6]–[8]
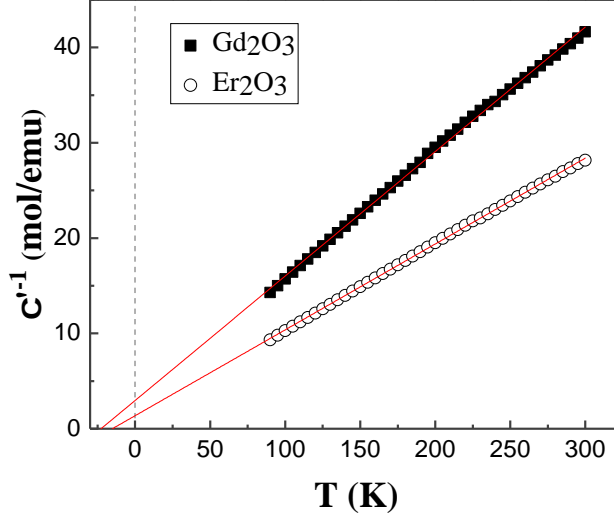
Figure 3.8: Inverse AC Susceptibility as a function of temperature for paramagnetic salts Er_2O_3 and Gd_2O_3 along with linear fitted curve to the experimental data.

3.6   Setup Calibration

The setup calibration was done at 133 Hz frequency using two paramagnetic salts - Gd_2O_3 and Er_2O_3, both of which have a known Curie constant and Temperature [53]. They are therefore used to calibrate the setup by fitting a linear equation through the data points and finding calibration constant using the Eq(1.5) given in chapter 1. This is done by normalizing the obtained signal by field and frequency of the primary coil, and the mass of the sample. The linear equation which fits these data points is now compared to the Curie-Weiss law, and the calibration constant is found out by matching the slope with the Curie constant and the intercept on the x-axis (temperature axis) with the Curie temperature of the salt (Fig(3.8)). The value of Curie constant and temperature obtained from the slope after calibrating and the literature values are compared in Table 3.1. As can be seen, these match well with the literature values.

Sample 1	C_{cal} (emu/mol K)	C_{lit}	θ_{cal} (K)	θ_{lit}
Er_2O_3	...	11.1	-15.2	-13.4
Gd_2O_3	7.6	8.3	-22.6	-18.4

Table 3.1: Setup calibration best fit parameters

3.7 Challenges Involved and Troubleshooting

The major challenges in constructing a low temperature experimental setup such as presented in this thesis and some of the salient points which are crucial for troubleshooting are discussed below.

1. The trickiest part involved in designing the setup was to hang the primary and the secondary coils which were wound on a quartz tube (Fig(3.7b)). This needs to be an easy-to-disassemble configuration, as well as Helium tight (such that Helium vapours do not escape and are sent to the Helium plant for liquefaction). In addition, if need be so the coil set should be taken out with ease. The idea to hang these glass tubes using two o-rings creating an effective kf coupling appears to be a viable option [61]. This states that such a configuration can attain ultra-high vacuum of up to 10^{-6} mbar with turbomolecular pump. Our setup achieves a high vacuum of 10^{-3} mbar with rotary vane pump and is sufficient for performing the experiments reported in this work. Better vacuum may be possible with a turbomolecular pump, but is not necessarily required.

2. The linear manual coil winding machine in the lab can only accommodate a maximum of 230 mm length of the material over which coil has to be wound. Since the coil itself is 160 mm (including hylam rings) in length, this leaves just 60 mm space from the top (10 mm used at bottom to hold the tube) where the quartz tube has to be fused to another longer tube. Quartz has a melting point of 1575 to 1725 ℃ [59]. It was important to confirm that the copper coil insulation (burning point 400 ℃) was be able to withstand its integrity after fusing the glass inserts, post winding the coils. This was checked by measuring the resistance of the coil before and after the fusing. It remained same indicating that the coil survived.

3. The whole setup was given for manufacturing using SS316. This is high quality stainless steel and in literature it is know to have less tendency to become magnetic upon machining than SS304 (conversion from austensitic to martensitic form). Unlike SS304, it also does not become magnetic upon repeated thermal cycling. However, when the manufactured cluster flange arrived, a few metallic parts were already magnetic. A few components became magnetic after thermal cycling. Ideally non-magnetic metallic parts are neede for low temperature insert. It appears that the insert was manufactured

with SS raw material which was not non-magnetic as desired. To avoid the risk of this happening again and because of shortage of time, this flange was replaced by an SS304 one which was immediately available and was much less magnetic. A new Aluminium (paramagnetic) flange will be given for manufacturing in the future, which will replace this one in the setup.

4. Procuring the correct size glass tube for the LHe Dewar, cutting it to the right side, and getting it closed from one end were the most difficult tasks in this project. Even more difficult was getting these silvered due to the lack of appropriate glass blowing facilities, hence this could not be done. For LHe runs a silvered He Dewar is needed (which could not be done during the course of this project).
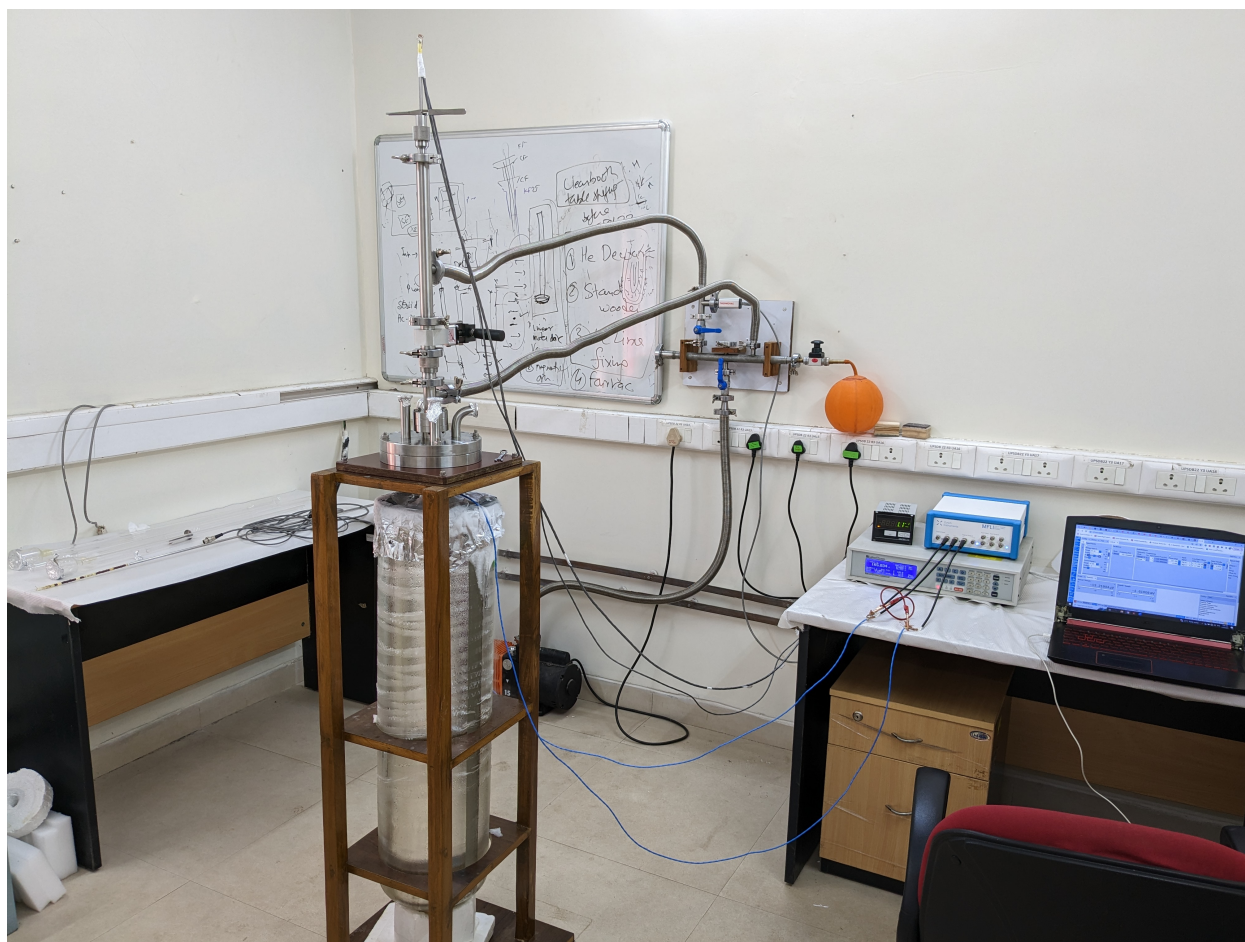
Figure 3.9: New LHe compatible AC-Susceptibility setup.

3.8   Work done on LN$_2$ AC-Susceptometer

The LN$_2$ AC-Susceptometer was constructed by Sayan Debnath, a senior BS-MS fifth year project student. To learn and get the feel of the instrument, I helped Ananth Kamath (a senior MS project student) perform various runs. Hands-on experience was obtained by opening and exploring the setup and getting the signal profile of the PRT inside the coils (data not included for simplicity). PID tuning of the new sample rod constructed was also performed and dry runs were independently performed. I also helped Ananth in calibrating the setup using Gd$_2$O$_3$ powder pellet.

Most importantly, AC susceptibility of CoF$_2$ Single Crystal was also measured on this existing setup down to LN$_2$ temperature (which has coils wound in hylam former). For comparison with the new quartz glass insert /coil setup, same sample was measured in the new setup. The results highlighting the improvement in the sensitivity will be discussed in the next chapter.

Chapter 4

AC Susceptibility data for CoF$_2$ Single Crystal in the Paramagnetic Region

CoF$_2$ is basically an AFM which crystallizes in tetragonal rutile structure. The Antiferromagnetic vector is along the c-direction [27]. This is unlike NiF$_2$ in which the antiferomagnetic vector lies in the basal plane and NiF$_2$ is know to be both Weak ferromagnetic and piezomagnetic [9], [11]. While the stress induced magnetic moments, and hence piezomagnetism, has been experimentally measured on CoF$_2$ [10], the spin canted state, without the application of external pressure in this compound is still controversial [10], [48]. On CoF$_2$ micro-crystallites, the DC magnetometry data, especially the remanence discussed in chapter 2, has already indicated that spin canting has a role to play in the magnetization dynamics of CoF$_2$ in the absence of pressure. The AFM transition of CoF$_2$ is around -32K, however, we could not perform LHe runs during the course of this project due to time limitations. Therefore, the AC-Susceptibility measurements on CoF$_2$ SC in the paramagnetic region (LN$_2$ temperatures) is discussed here. For this purpose, Laue pattern was recorded and AC susceptibility was recorded along the a-axis. There are anomalies already reported in the DC susceptibility measuerements of CoF$_2$ [46]–[49], therefore DC susceptibility data in the paramagnetic region will be crucial.
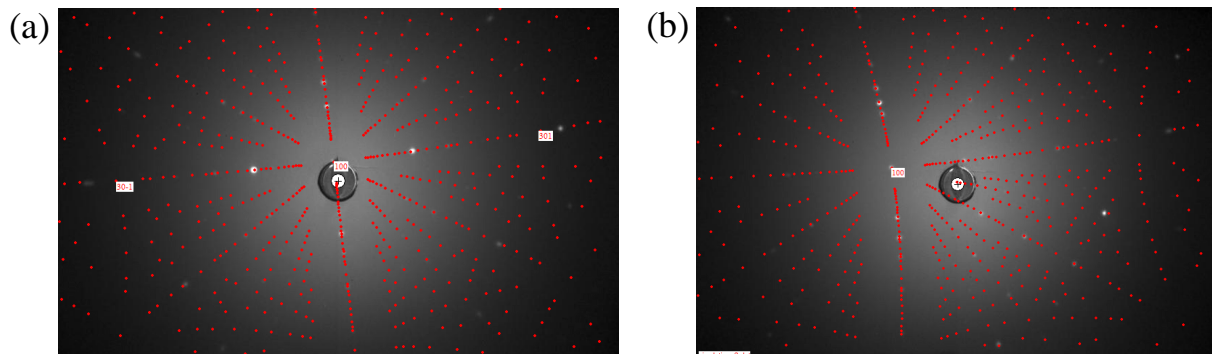
Figure 4.1: Laue X-ray diffraction pattern (white spots) and the simulated pattern superimposed on it (red spots), (a) When one of the faces of the CoF_2 was perpendicular to the beam direction, and (b) When it is rotated to the left.

4.1 Laue X-Ray Diffraction

To determine the axes of the CoF_2 SC, Laue X-Ray diffraction was performed on it and the pattern was examined. In Laue diffraction, white X-Ray is emitted from the source (tungsten in the instrument at IISER Pune), these form a reciprocal lattice map after back-scattering from the lattice onto the imaging screen. The wavelength range in the Laue diffractometer at IISER Pune is 0.35 Å- 2.50 Å(Fig(4.2a)). Given the space group and the lattice parameters of the SC, the pattern obtained can be simulated on a computer (software used is Orient Express). This simulated pattern is then compared to the obtained pattern to determine the crystallographic axes of the SC. The X-ray diffraction and axis determination was done by Sagar, a PhD student at Dr. Surjeet's lab at IISER Pune.

Fig(4.1) presents the diffraction pattern and the simulated pattern superimposed on it when one of the faces of the CoF_2 was perpendicular to the beam direction, and when it is rotated to the left. These patterns were obtained after keeping the SC in X-rays for 10 mins. Using both these images and matching the arcs in the pattern obtained, the axis parallel to the beam direction was found out to be a-axis. Some mismatch in the arc may be due to error in the distance taken from the screen to the CoF_2 SC, because the distance had to be adjusted by hand. In such cases the simulated pattern can be rotated a little to match one arc or the other, and the whole arc must fall on the experimentally obtained spots.

Once the crystal axis has been determined, we performed AC-Susceptibility measurements along the a-axis. These data are discussed in next section.
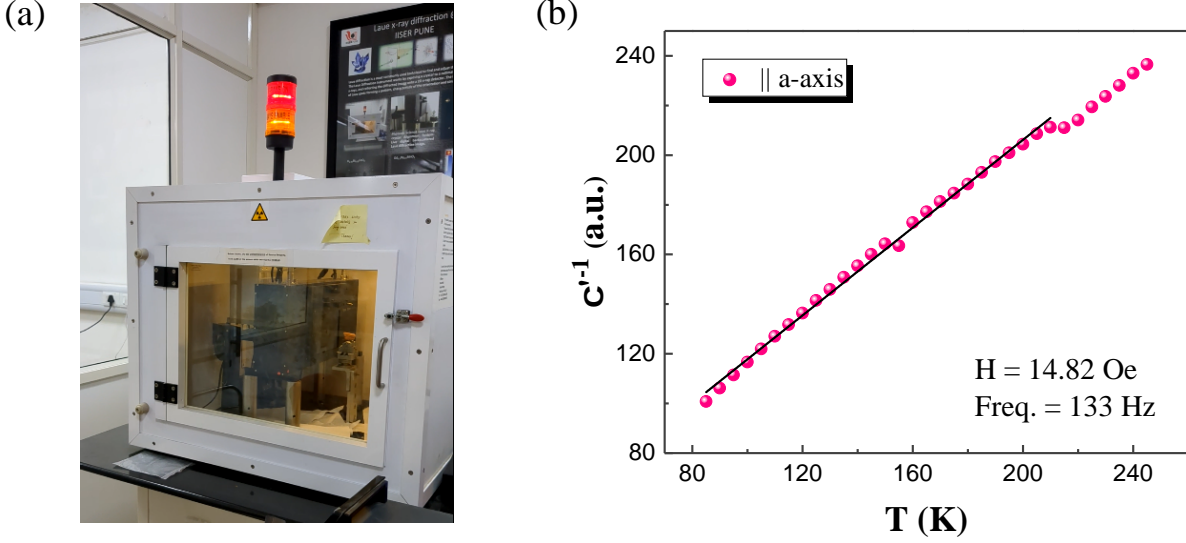
Figure 4.2: (a) Laue X-Ray diffraction set-up. (b) Inverse of linear AC susceptibility of CoF_2 SC as a function of temperature measured at RMS field of 14.82 Oe, and frequency 133 Hz in paramagnetic region.

4.2 AC Susceptibility data for field parallel to the a-axis

The AC-Susceptibility data in the paramagnetic region are obtained at AC field of 14.82 Oe (RMS), and 133 Hz (Fig(4.2b)). These data are obtained in the temperature range of 77K to 240K. As evident from Fig(4.2b) this data is in arbitrary units. To convert it to real units a dry run is needed. This is done to subtract the contribution of the coil off set , as well as for estimating the undesired signal arising from (i) heater and temperature sensor etc. (ii) any magnetic contribution arising from the metallic parts. The data for dry run showed some anomoly which could not be resolved, hence we have not used this data for the estimation of error free susceptibility of CoF_2. Therefore, the data is shown in arbitrary units. It is also to be noted that for CoF_2, especially in the paramagnetic region, the low field AC Susceptibility measurement leads to a very small value. Due to this reason, precise measurements of the dry run is necessary. And hence this measurement needs repetition.

However, the qualitative behaviour of the susceptibility of CoF_2 in the paramagnetic region appears to be linear as is expected . As can be seen from Fig(4.2b), parallel susceptibility follow Curie-Weiss law from 77K to 240K. A small feature in the susceptibility appears
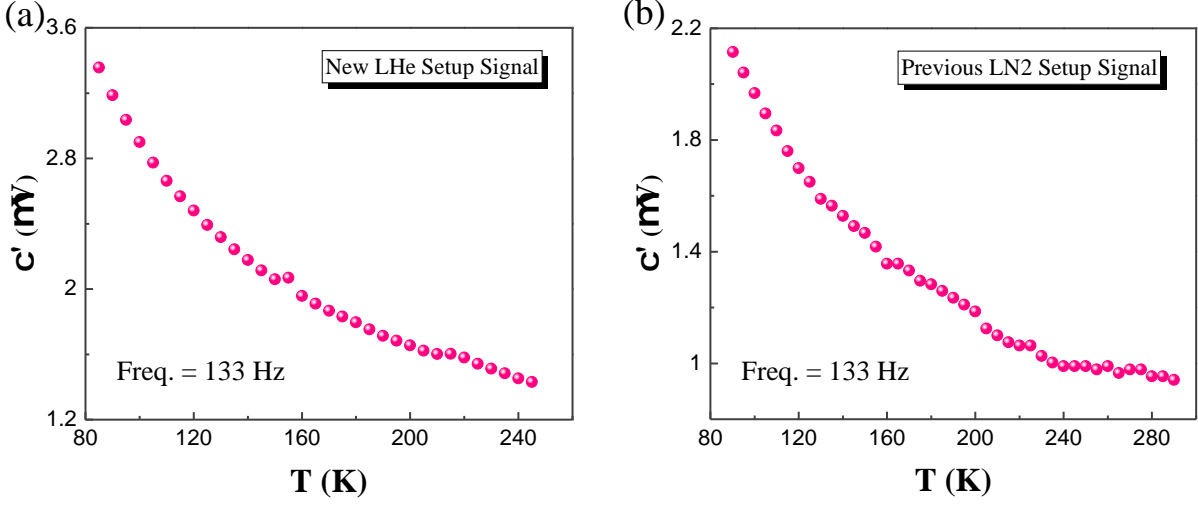
Figure 4.3: Linear AC susceptibility signal of CoF_2 SC normalized by the field applied and at frequency 133 Hz in paramagnetic region for (a) New LHe Setup, (b) LN_2 Setup.

to arise from the stretched teflon, which is wound over the SC. The stretched teflon is reported to generate ferromagnetic like features due to carbon dangling bonds [62]. However, this factor needs to be further investigated.

4.3   Sensitivity improvement over LN_2 Setup

Fig(4.3) provides the signals obtained in the LN_2 setup in the lab and the new setup for the same CoF_2 SC normalized by the field applied in both the setups. It can be seen that the signal in the new setup is about 1.6 times that in the other setup in which coil was wound over a Hylam former. This is due to the coil being wound directly on the quartz tube resulting in a smaller diameter, and hence an increased filling factor (sample is closer to the coil), which would result in a greater signal voltage (Eq(1.5)). We need repeat measurements especially for the dry run to confirm the enhancement in the sensitivity.

Chapter 5

Conclusion

In this work we have explored Single Ion Anisotropy (SIA) driven spin canted systems, CoF_2 and NiF_2. Both these systems in the micro-crystallite form have been explored through DC magnetometry, specially through the remanence measurements. It is emphasized that the Dzyaloshinskii Moriya Interaction (DMI) driven systems (such as α-Fe_2O_3) exhibit some features in remanence which appear to be exclusive to spin canted systems [5], [7]. One part of the thesis is devoted to exploring whether these features appear in SIA driven systems as well. The M-H isotherms for both samples show opening of the loop indicating presence of weak ferromagnetism. The M_{FC} vs T curves also points towards a Weak Ferromagnet (WFM) state, with magnetization and Thermo-remanent Magnetization (TRM) both higher in magnitude for CoF_2 than NiF_2. This is strikingly similar to DMI driven WFMs where substance with lower T_N has higher TRM and magnetization, but lower TRM retention [5]–[8]. We conclude that both CoF_2 and NiF_2 exhibit time-stable remanence just like DMI driven WFMs which is intimately connected to the spin canted phase. It is important to note here that these systems are not nano-scaled, and are not even glassy systems or superparamagnets which can show such relaxation dynamics [50], [51]. But unlike the DMI systems these do not show a peak-like feature in their remanence, at least for fields upto 10 kOe. We also find that the field dependence of these remanence can help us isolate DMI driven from SIA driven WFMs. In addition to this, a long standing issue with CoF_2 has been whether it is a spin canted system in the absence of external pressure [10], [48]. Our DC magnetometry data reveals that spin canting appears to be intimately connected to the magnetic properties of CoF_2. The DC susceptibility data shows highly non-linear behaviour

in NiF_2, while it shows only slight non-linearity in CoF_2 sample. All these interesting properties coupled with slow relaxation dynamics make these ideal candidates for performing AC susceptibility measurements to further probe them and try to find a fingerprint which separates them from other systems.

To explore the unusual magnetization dynamics in these systems, a sensitive AC - Susceptibility bridge – compatible for measurements down to Liquid Helium (LHe) – is designed and fabricated (since the transitions of CoF_2 and NiF_2 are below Liquid Nitrogen (LN_2) temperature). This involved coming up with a removable coil setup design, which would still keep the whole system sealed such that the evaporated He can be collected back at the He liquefaction plant. The setup needed an increased sensitivity (over the LN_2 setup) to be able to detect the sample's signal and take proper measurements, especially in the paramagnetic region. Hence, the pickup coil is made to be a part of the low temperature insert itself (by winding it on the quartz insert), and this has led to a significant enhancement in the sensitivity of the setup over the ones reported in literature [53], [54]. The coils made are then characterised by finding the field dependence of their offset and the setup is calibrated down to LN_2 using paramagnetic salts with known Curie constant. The sample rod associated with the setup also had to redone at various parts and the setup could start taking readings after its offset was removed. The LHe temperature run could not be performed during the course of this project.

The initial AC susceptibility data taken on CoF_2 Single Crystal (SC) is reported which shows linearity in the paramagnetic region. The curve appears to follow Curie-Weiss law in the temperature region where the sample was probed (77K to 250K). Further measurements on both NiF_2 and CoF_2 SC are planned at different fields, frequencies and orientations of the SCs till LHe temperatures (4.2 K). These can also be cooled while applying a DC field and changes in the system response will be observed.

5.1 Future Prospects

The glass tubes for LHe Dewar need to be attached to the aluminium flange after it is manufactured, and the setup will be tested with LN_2 rigorously before the LHe run starts. We also intend to calibrate the setup down to LHe temperature and perform measurements on both CoF_2 and NiF_2 SC. It would be interesting to see the behaviour of non-linear harmonics

in these systems. The setup also needs to be automated for ease of data collection. Overall, exciting results await in the future once the LHe runs start on the setup.

Bibliography

[1] S.-W. Cheong and M. Mostovoy, "Multiferroics: A magnetic twist for ferroelectricity," *Nature Materials*, vol. 6, no. 1, pp. 13–20, 2007. DOI: `10.1038/nmat1804`.

[2] M. Shiranzaei, J. Fransson, H. Cheraghchi, and F. Parhizgar, "Nonlinear spin susceptibility in topological insulators," *Physical Review B*, vol. 97, no. 18, 2018. DOI: `10.1103/physrevb.97.180402`.

[3] S. Heinze, K. von Bergmann, M. Menzel, *et al.*, "Spontaneous atomic-scale magnetic skyrmion lattice in two dimensions," *Nature Physics*, vol. 7, no. 9, pp. 713–718, 2011. DOI: `10.1038/nphys2045`.

[4] M. Bode, M. Heide, K. von Bergmann, *et al.*, "Chiral magnetic order at surfaces driven by inversion asymmetry," *Nature*, vol. 447, no. 7141, pp. 190–193, 2007. DOI: `10.1038/nature05802`.

[5] A. Kapoor, A. B. Dey, C. Garg, and A. Bajpai, "Enhanced magnetism and time-stable remanence at the interface of hematite and carbon nanotubes," *Nanotechnology*, vol. 30, no. 38, p. 385 706, 2019. DOI: `10.1088/1361-6528/ab27ec`.

[6] A. Bajpai, R. Klingeler, N. Wizent, A. K. Nigam, S.-W. Cheong, and B. Büchner, "Unusual field dependence of remanent magnetization in granular CrO_2: The possible relevance of piezomagnetism," *Journal of Physics: Condensed Matter*, vol. 22, no. 9, p. 096 005, 2010. DOI: `10.1088/0953-8984/22/9/096005`.

[7] N. Pattanayak, A. Bhattacharyya, S. Chakravarty, and A. Bajpai, "Weak ferromagnetism and time-stable remanence in hematite: Effect of shape, size and morphology," *Journal of Physics: Condensed Matter*, vol. 31, no. 36, p. 365 802, 2019. DOI: `10.1088/1361-648x/ab251c`.

[8] N. Pattanayak, A. Bhattacharyya, A. K. Nigam, S.-W. Cheong, and A. Bajpai, "Quasistatic remanence in dzyaloshinskii-moriya interaction driven weak ferromagnets and piezomagnets," *Physical Review B*, vol. 96, no. 10, 2017. DOI: `10.1103/physrevb.96.104422`.

[9] V. Loktev, "On the theory of static magnetic susceptibility of NiF_2," *Physics Letters A*, vol. 81, no. 9, pp. 533–535, 1981. DOI: `10.1016/0375-9601(81)90460-6`.

[10] A. S. Borovik-Romanov, "Piezomagnetism in the antiferromagnetic fluorides of cobalt and manganese," *Journal of Experimental and Theoretical Physics (U.S.S.R)*, vol. 38, pp. 1088–1098, 1960.

[11] R. G. Shulman, "Nuclear magnetic resonance and magnetic ordering in NiF_2," *Physical Review*, vol. 121, no. 1, pp. 125–143, 1961. DOI: `10.1103/physrev.121.125`.

[12] T. Moriya, "Weak ferromagnetism," in *Magnetism*, G. T. Rado and H. Suhl, Eds. Academic Press, 1963, vol. 1, pp. 85–125.

[13] A. S. Borovik-romanov, "Piezomagnetism, linear magnetostriction and magnetooptic effect," *Ferroelectrics*, vol. 162, no. 1, pp. 153–159, 1994. DOI: `10.1080/00150199408245101`.

[14] C. V. Topping and S. J. Blundell, "A.c. susceptibility as a probe of low-frequency magnetic dynamics," *Journal of Physics: Condensed Matter*, vol. 31, no. 1, p. 013 001, 2018. DOI: `10.1088/1361-648x/aaed96`.

[15] M. Nikolo, "Superconductivity: A guide to alternating current susceptibility measurements and alternating current susceptometer design," *American Journal of Physics*, vol. 63, no. 1, pp. 57–65, 1995. DOI: `10.1119/1.17770`.

[16] S. Blundell, *Magnetism in condensed matter*. Oxford University Press, 2014.

[17] A. Awan, H. Truong, and R. J. Lancashire, *Crystal field theory*, May 2021. [Online]. Available: `https://chem.libretexts.org/Bookshelves/Inorganic_Chemistry/Supplemental_Modules_and_Websites_%5C%28Inorganic_Chemistry%5C%29/Crystal_Field_Theory/Crystal_Field_Theory`.

[18] C. M. Hurd, "Varieties of magnetic order in solids," *Contemporary Physics*, vol. 23, no. 5, pp. 469–493, 1982. DOI: `10.1080/00107518208237096`.

[19] V. Iacovacci, G. Lucarini, L. Ricotti, and A. Menciassi, "Magnetic field-based technologies for lab-on-a-chip applications," *Lab-on-a-Chip Fabrication and Application*, 2016. DOI: `10.5772/62865`.

[20] I. Dzyaloshinsky, "A thermodynamic theory of "weak" ferromagnetism of antiferromagnetics," *Journal of Physics and Chemistry of Solids*, vol. 4, no. 4, pp. 241–255, 1958. DOI: 10.1016/0022-3697(58)90076-3.

[21] T. Moriya, "Anisotropic superexchange interaction and weak ferromagnetism," *Physical Review*, vol. 120, no. 1, pp. 91–98, 1960. DOI: 10.1103/physrev.120.91.

[22] P. J. Brown and J. B. Forsyth, "A neutron diffraction study of weak ferromagnetism in nickel fluoride," *Journal of Physics C: Solid State Physics*, vol. 14, no. 33, pp. 5171–5184, 1981. DOI: 10.1088/0022-3719/14/33/023.

[23] T. Hahn, in *International Tables For Crystallography*. Springer, 2002, pp. 468–551.

[24] A. H. Cooke, K. A. Gehring, and R. Lazenby, "The magnetic properties of NiF_2," *Proceedings of the Physical Society*, vol. 85, no. 5, pp. 967–977, 1965. DOI: 10.1088/0370-1328/85/5/315.

[25] T. G. Phillips, R. L. Townsend, and R. L. White, "Piezomagnetism of α-Fe_2O_3 and the magnetoelastic tensor of Fe^{3+} in Al_2O_3," *Phys. Rev.*, vol. 162, pp. 382–388, 2 Oct. 1967. DOI: 10.1103/PhysRev.162.382.

[26] J. Strempfer, U. Rütt, S. P. Bayrakci, T. Brückel, and W. Jauch, "Magnetic properties of transition metal fluorides MF_2 (M = Mn, Fe, Co, Ni) via high-energy photon diffraction," *Physical Review B*, vol. 69, no. 1, 2004. DOI: 10.1103/physrevb.69.014417.

[27] A. N. Bazhan and C. Bazan, "Weak ferromagnetism in CoF_2 and NiF_2," *Journal of Experimental and Theoretical Physics*, vol. 42, no. 5, pp. 898–904, 1975.

[28] R. L. Fagaly, "Superconducting quantum interference device instruments and applications," *Review of Scientific Instruments*, vol. 77, no. 10, p. 101 101, 2006. DOI: 10.1063/1.2354545.

[29] J. Clarke, "Squids," *Scientific American*, vol. 271, no. 2, pp. 46–53, 1994. DOI: 10.1038/scientificamerican0894-46.

[30] M. Tinkham, "6.5 squid devices," in *Introduction to superconductivity*, 2nd ed. Dover Publications Inc., 1996, pp. 224–226.

[31] A. Edgar and J. W. Quilty, "A mutual inductance apparatus for measuring magnetic susceptibility and electrical conductivity," *American Journal of Physics*, vol. 61, no. 10, pp. 943–946, 1993. DOI: 10.1119/1.17373.

[32]   A. Banerjee, A. Bajpai, and S. Nair, "Probing magnetic phases in different systems using linear and non linear susceptibility," in *Frontiers in Magnetic Materials*, A. V. Narlikar, Ed. Berlin, Heidelberg: Springer Berlin Heidelberg, 2005, pp. 43–69, ISBN: 978-3-540-27284-7. DOI: `10.1007/3-540-27284-4_2`.

[33]   M. I. Youssif, A. A. Bahgat, and I. A. Ali, "Ac magnetic susceptibility technique for the characterization of high temperature superconductors," *Egyptian Journal of Solids*, vol. 23, no. 2, pp. 231–250, 2000. DOI: `10.21608/ejs.2000.151732`.

[34]   D. Gatteschi, R. Sessoli, and J. Villain, "3.1.5 ac susceptometry," in *Molecular nano-magnets*. Oxford Univ. Press, 2011, pp. 69–71.

[35]   L. Holleis, J. C. Prestigiacomo, Z. Fan, *et al.*, "Anomalous and anisotropic nonlinear susceptibility in the proximate kitaev magnet $\alpha - \mathrm{RuCl}_3$," *npj Quantum Materials*, vol. 6, no. 1, 2021. DOI: `10.1038/s41535-021-00364-z`.

[36]   A. Palmer and W. Jauch, "On the domain structure in NiF_2: A γ-ray diffraction study," *Solid State Communications*, vol. 77, no. 1, pp. 95–97, 1991. DOI: `10.1016/0038-1098(91)90435-x`.

[37]   L. M. Matarrese and J. W. Stout, "Magnetic anisotropy of NiF_2," *Physical Review*, vol. 94, no. 6, pp. 1792–1793, 1954. DOI: `10.1103/physrev.94.1792`.

[38]   J. W. Stout and E. Catalano, "Thermal anomalies associated with the antiferromagnetic ordering of FeF_2, CoF_2, NiF_2," *Physical Review*, vol. 92, no. 6, pp. 1575–1575, 1953. DOI: `10.1103/physrev.92.1575`.

[39]   P. A. Joy, P. S. A. Kumar, and S. K. Date, "The relationship between field-cooled and zero-field-cooled susceptibilities of some ordered magnetic systems," *Journal of Physics: Condensed Matter*, vol. 10, no. 48, p. 11 049, Dec. 1998. DOI: `10.1088/0953-8984/10/48/024`.

[40]   J. Liu, X. Cheng, F. Tong, and X. Miao, "Spin-glass behavior and anomalous magnetoresistance in ferromagnetic $\mathrm{Ge}_{1-x}\mathrm{Fe}_x\mathrm{Te}$ epilayer," *Journal of Applied Physics*, vol. 116, no. 4, Jul. 2014, 043901, ISSN: 0021-8979. DOI: `10.1063/1.4890987`.

[41]   M. D. Mukadam, S. M. Yusuf, P. Sharma, S. K. Kulshreshtha, and G. K. Dey, "Dynamics of spin clusters in amorphous $\mathrm{Fe}_2\mathrm{O}_3$," *Phys. Rev. B*, vol. 72, p. 174 408, 17 Nov. 2005. DOI: `10.1103/PhysRevB.72.174408`.

[42]   A. S. Borovik-Romanov, A. N. Bazhan, and N. M. Kreines, "The weak ferromagnetism of NiF_2," *Zh. Eksp. Teor. Fiz*, vol. 64, pp. 1367–1382, 1973.

[43] D. N. Astrov, A. S. Borovik-Romanov, and M. P. Orlova, "Magnetic properties of cobalt fluoride in the antiferromagnetic state," *Journal of Experimental and Theoretical Physics (U.S.S.R.)*, vol. 33, pp. 812–815, 1957.

[44] V. I. Ozhogin, "The antiferromagnets coco $_3$, CoF_2, and $FeCO_3$ in strong fields," *Journal of Experimental and Theoretical Physics (U.S.S.R)*, vol. 45, pp. 1156–1158, 1963.

[45] P. Sheng, Y. Xie, Y. Bai, *et al.*, "Magnetoelastic anisotropy of antiferromagnetic materials," *Applied Physics Letters*, vol. 115, no. 24, Dec. 2019, 242403, ISSN: 0003-6951. DOI: 10.1063/1.5128141.

[46] M. E. Lines, "Magnetic properties of CoF_2," *Phys. Rev.*, vol. 137, A982–A993, 3A Feb. 1965. DOI: 10.1103/PhysRev.137.A982.

[47] J. W. Stout and L. M. Matarrese, "Magnetic anisotropy of the iron-group fluorides," *Rev. Mod. Phys.*, vol. 25, pp. 338–343, 1 Jan. 1953. DOI: 10.1103/RevModPhys.25.338.

[48] U. Köbler, I. Radelytskyi, and H. Szymczak, "Relevant crystal field interaction in the magnetically ordered state," *Journal of Magnetism and Magnetic Materials*, vol. 474, pp. 254–268, 2019, ISSN: 0304-8853. DOI: https://doi.org/10.1016/j.jmmm.2018.11.028.

[49] T. Nakamura and H. Taketa, "On the para- and antiferromagnetic states of cobalt fluoride," *Progress of Theoretical Physics*, vol. 13, no. 2, pp. 129–147, 1955. DOI: 10.1143/ptp.13.129.

[50] M. J. Benitez, O. Petracic, H. Tüysüz, F. Schüth, and H. Zabel, "Fingerprinting the magnetic behavior of antiferromagnetic nanostructures using remanent magnetization curves," *Physical Review B*, vol. 83, no. 13, 2011. DOI: 10.1103/physrevb.83.134424.

[51] K. Binder and A. P. Young, "Spin glasses: Experimental facts, theoretical concepts, and open questions," *Reviews of Modern Physics*, vol. 58, no. 4, pp. 801–976, 1986. DOI: 10.1103/revmodphys.58.801.

[52] T. Moriya, "Theory of magnetism of NiF_2," *Physical Review*, vol. 117, no. 3, pp. 635–647, 1960. DOI: 10.1103/physrev.117.635.

[53] A. Bajpai and A. Banerjee, "An automated susceptometer for the measurement of linear and nonlinear magnetic ac susceptibility," *Review of Scientific Instruments*, vol. 68, no. 11, pp. 4075–4079, Nov. 1997, ISSN: 0034-6748. DOI: 10.1063/1.1148349.

[54] A. Bajpai and S. Debnath, "Exploring linear and nonlinear ac-susceptibilities in a single crystal of alpha-fe2o3 around the morin transition using a home-built ac susceptometer," *MS Thesis, IISER Pune*, Apr. 2022. [Online]. Available: `http://dr.iiserpune.ac.in:8080/xmlui/handle/123456789/6941`.

[55] J. W. Ekin, *Experimental techniques for low-temperature measurements: Cryostat design, material properties, and superconductor critical-current testing.* Oxford University Press, 2015.

[56] F. J. Norton, "Helium diffusion through glass," *Journal of the American Ceramic Society*, vol. 36, no. 3, pp. 90–96, 1953. DOI: `10.1111/j.1151-2916.1953.tb12843.x`.

[57] C. Lane and H. A. Fairbank, "Pyrex dewars for liquid helium," *Review of Scientific Instruments*, vol. 18, no. 7, pp. 522–522, 1947.

[58] A. Mayr, D. Kißkalt, A. Lomakin, K. Graichen, and J. Franke, "Towards an intelligent linear winding process through sensor integration and machine learning techniques," *Procedia CIRP*, vol. 96, pp. 80–85, 2021. DOI: `10.1016/j.procir.2021.01.056`.

[59] N. Zhang, X. Yu, A. Pradhan, and A. J. Puppala, "Thermal conductivity of quartz sands by thermo-time domain reflectometry probe and model prediction," *Journal of Materials in Civil Engineering*, vol. 27, no. 12, p. 04 015 059, 2015. DOI: `10.1061/(ASCE)MT.1943-5533.0001332`.

[60] C. P. Khattak and F. Schmid, "Growth of the world's largest sapphire crystals," *Journal of Crystal Growth*, vol. 225, no. 2-4, pp. 572–579, 2001. DOI: `10.1016/s0022-0248(01)00955-1`.

[61] *One end closed quartz tube (*800 OD $\times$ 73 ID $\times$ 200 L*, mm) W/ CF flange for ultra-hi vacuum & limit;* $5 \times 10E - 6$ *torr.* [Online]. Available: `https://www.mtixtl.com/EQ-CFF-80.aspx`.

[62] Y. Ma, Y. Lu, J. Yi, *et al.*, "Room temperature ferromagnetism in teflon due to carbon dangling bonds," *Nature Communications*, vol. 3, no. 1, 2012. DOI: `10.1038/ncomms1689`.